Pore Structure Dependence of Transport and Fracture in Pervious Concretes

by

Benjamin Rehder

A Thesis Presented in Partial Fulfillment
of the Requirements for the Degree
Master of Science

Approved May 2013 by the
Graduate Supervisory Committee:

Narayanan Neithalath, Chair
Barzin Mobasher
Subramaniam Rajan

ARIZONA STATE UNIVERSITY

August 2013

ABSTRACT

Properties of random porous material such as pervious concrete are strongly dependant on its pore structure features. This research deals with the development of an understanding of the relationship between the material structure and the mechanical and functional properties of pervious concretes.

The fracture response of pervious concrete specimens proportioned for different porosities, as a function of the pore structure features and fiber volume fraction, is studied. Stereological and morphological methods are used to extract the relevant pore structure features of pervious concretes from planar images. A two-parameter fracture model is used to obtain the fracture toughness (K_{IC}) and critical crack tip opening displacement ($CTOD_c$) from load-crack mouth opening displacement (CMOD) data of notched beams under three-point bending. The experimental results show that K_{IC} is primarily dependent on the porosity of pervious concretes. For a similar porosity, an increase in pore size results in a reduction in K_{IC}. At similar pore sizes, the effect of fibers on the post-peak response is more prominent in mixtures with a higher porosity, as shown by the residual load capacity, stress-crack extension relationships, and G_R curves. These effects are explained using the mean free spacing of pores and pore-to-pore tortuosity in these systems. A sensitivity analysis is employed to quantify the influence of material design parameters on K_{IC}.

This research has also focused on studying the relationship between permeability and tortuosity as it pertains to porosity and pore size of pervious concretes. Various

ideal geometric shapes were also constructed that had varying pore sizes and porosities. The pervious concretes also had differing pore sizes and porosities. The permeabilities were determined using three different methods; Stokes solver, Lattice Boltzmann method and the Katz-Thompson equation. These values were then compared to the tortuosity values determined using a Matlab code that uses a pore connectivity algorithm. The tortuosity was also determined from the inverse of the conductivity determined from a numerical analysis that was necessary for using the Katz-Thompson equation. These tortuosity values were then compared to the permeabilities. The pervious concretes and ideal geometric shapes showed consistent similarities between their tortuosities and permeabilities.

ACKNOWLEDGMENTS

I would like to thank my advisor, Dr. Narayanan Neithalath for his constant guidance and support during the course of my work at Arizona State University. His enthusiasm towards the quality of work has made graduate school a challenging, rewarding as well as an enjoyable experience for me. I would also like to thank my committee members Dr. Subramaniam Rajan and Dr. Barzin Mobasher for agreeing to examine my thesis work.

I gratefully acknowledge the financial support from the National Science Foundation and Arizona State University for carrying out this research.

I sincerely thank all my friends and lab mates which have made this thesis possible. I would also like to give a special thanks to Kingston Bahn for assisting me with conducting many experiments and analysis in the summer of 2012. My deepest gratitude is towards my parents for their underlying love and encouragement.

TABLE OF CONTENTS

Page

LIST OF TABLES

Page

LIST OF FIGURES

1 CHAPTER 1: INTRODUCTION

1.1 General

Pervious concrete (also known as enhanced porosity concrete) is proportioned using gap-grading the coarse aggregates and eliminating sand so as to create a high level of porosity (20-30%) and a network of large open pores (2-6 mm) in the material. The environmental benefits of pervious concretes have been well recognized with respect to stormwater run-off reduction and recharging groundwater (Tennis, Leming, & Akers, 2004)("Report on Pervious Concrete (ACI 522R – 10)," 2010)(Omkar Deo & Neithalath, 2010), and tire-pavement interaction noise reduction (Marolf et al., 2004)(Olek et al., 2003)(Neithalath, Marolf, Weiss, & Olek, 2005) when used as surface courses in parking lots and pavements. These benefits have resulted in pervious concretes being increasingly used for load-bearing structures including pavements and overlays that require higher mechanical and durability properties. Unlike conventional concretes which are generally designed for the lowest possible porosity, pervious concretes are designed for a non-minimal porosity, and a high degree of interconnectedness in the pore structure so as to facilitate its functional demands. This, in turn, detrimentally affects the mechanical and durability properties of the material. A few studies have reported methods to improve the compressive strength (Huang, Wu, Shu, & Burdette, 2010)(Agar-Ozbek, Weerheijm, Schlangen, & van Breugel, 2013)(Yang & Jiang, 2003) and freeze-thaw durability (Kevern, Schaefer, Wang, & Suleiman, 2008) of pervious concretes.

The major determinant of all the properties of pervious concretes is its pore structure, which generally has been considered to include the total pore volume fraction or the porosity, the characteristic pore sizes, and the degree of connectivity or tortuosity in the pore system. These pore structure features depend on the material design parameters (water-to-cement ratio, aggregate size, paste content, and degree of compaction). Traditionally, pervious concretes have been designed based on a trial-and-error approach, but a sophisticated particle-packing based approach that relies on the virtual packing densities and volume fractions of the mixture components and the actual packing density of the mixture has been recently developed (Milani S. Sumanasooriya, Deo, & Neithalath, 2012)(Omkar Deo & Neithalath, 2011). Extensive characterization of the pore structure in pervious concretes as a function of their material design parameters have been published (Armatas, Salmas, Louloudi, Androutsopoulos, & Pomonis, 2003)(M. S Sumanasooriya & Neithalath, 2011)(M. Sumanasooriya & Neithalath, 2009), and the influence of pore structure on the mechanical (Omkar Deo & Neithalath, 2010)(Omkar Deo & Neithalath, 2011)(Milani S. Sumanasooriya, Deo, & Neithalath, 2009) and transport (Haselbach, Valavala, & Montes, 2006)(Neithalath, Bentz, & Sumanasooriya, 2010)(Neithalath, Weiss, & Olek, 2006) properties of pervious concretes have been brought out through experimental means and computer simulations of reconstructed three-dimensional structures (M. Sumanasooriya, Bentz, & Neithalath, 2010)(Bentz, 2008).

This research investigates the influence of the pore structure of pervious concretes and the incorporation of fibers on its fracture behavior. This is important because, as

explained earlier, pervious concretes are increasingly being subjected to load-carrying applications. In a random heterogeneous two-phase material like pervious concrete with a dominant pore phase, it is expected that the pore structure (including the total pore volume, characteristic sizes, representative pore spacing in three dimensions, and pore-to-pore tortuosity) and its interaction with fibers influences the crack propagation resistance of the material. In this study, the fracture response of notched beams in three-point bending is characterized using an effective elastic crack approach (the two-parameter fracture model). The pore structure features of pervious concretes proportioned for different desired porosities are extracted using stereological and morphological principles (M. Sumanasooriya & Neithalath, 2009)(Coster & Chermant, 2001) either from planar images or three-dimensional structures reconstructed from planar images. The combined influence of pore structure features and fiber volume on the fracture behavior of pervious concretes is examined so as to facilitate rational design of the material structure for desired performance features. A statistical model combined with a Monte-Carlo based feature sensitivity prediction method is reported, that helps ascertain the relative sensitivity of pore structure features and fiber content on fracture toughness. A fracture energy release rate (G_f) based on non linear fracture mechanics models for quasi-brittle materials, and is classified as a fictitious crack approach, was determined for various types of pervious concrete and with varying amount of fibers (Shah, Swartz, & Ouyang, 1995)(Wittmann, 2002)(Hillerborg, Modeer, & Petersson, 1976).

1.2 Objectives of the Study

The major objectives of this study are listed below:

1. To understand a relationship between the permeability and tortuosity of pervious concretes and how they compare to ideal geometric shapes.
2. To explore and model and the influence of fibers and pore structure features on the fracture behavior of pervious concretes.
3. To explore and model and the influence of fibers and pore structure features on the energy release rate of pervious concrete.

.

2 CHAPTER 2: LITERATURE REVIEW OF 2D PORE CHARACTERTIZATION, 3D RECONSTRUCTION AND MODELING OF PERMEABILITY, ELASTICITY, AND FRACTURE MECHANICS OF ENHANCED POROSITY CONCRETE

2.1 General

The use of pervious concretes is being recognized in many parts of the world due to the many benefits in regards to sustainability offered by this material. Some of the more important applications are the reduction of storm water runoff and recharging of groundwater when used as a paving material for parking lots, low volume pavements, and sidewalks (Neithalath, Sumanasooriya, & Deo, 2010). Many of the performance characteristics of pervious concretes are still not fully understand despite its growing use. Among them is pore characteristics and their influence on the mechanical behavior which is the main focus of this research. A literature review based on past studies of pore characterization, permeability, elasticity, and fracture mechanics of enhanced porosity concrete is presented in this chapter.

2.2 2D Pore Characterization

This section explains the theory and methods for characterizing the pores in enhanced porosity concrete (EPC) using 2 dimensional images and pictures.

2.2.1 Image Processing

Image processing is important for studying images of concrete so that the features of interest can be captured and analyzed. There are several software packages available to transform grayscale pictures into binary images which enhances the contrast between the features of interest such as pores and cracks. One such software is Fiji which is freely downloadable from http://sourceforge.net/projects/fiji-bi/. (Soroushian & Elzafraney, 2005)

2.2.2 Stereological Methods

Image analysis is broadly defined as extraction of useful data from a digital image. It can be used to quantify different compounds of concrete as well as characterize the pore structure. (Mouret, Ringot, & Bascoul, 2001) Stereology can defined as a body of mathematical methods which relate 3d parameters that define the structure to 2d measurements obtained from digital image representations of perpendicular cross sections of the specimen of interest. It is an unbiased statistical method used to characterize the relative number, length, surface area, and volume of features in a microstructure without assumptions concerning size, shape, orientation, or location of the features. In practice, it is a technique that allows the accurate estimation of three-dimensional structural parameters and their standard deviations from two-dimensional projections. (Liddel, Summers, & Gokhale, 2003)

2.2.3 Pore size characterization from area histogram

The most common method to characterize pores is to use an area histogram to extract information on the pore size distribution from image analysis of planar sections.

Each pore is considered an individual feature and its area is found by counting the number of pixels contained within it. Its equivalent diameter is found by relating this area to the formula $A=pi*d^2/4$. This method can cause erroneous results when there are highly connected pores. An effective pore size (d_{50}) is defined as the pore size corresponding to 50% of the cumulative frequency distribution. (M. Sumanasooriya & Neithalath, 2009)

2.2.4 Lineal Analysis

A lineal analysis consists of taking a two phase region of a 2d images and having one region be represented by equally spaced lines and the other region be of a solid color. The area fraction of the pores can be found by taking the total length of the line segments and dividing by the total length of lines if they covered the entire graph. (Stjernberg, 1969)

2.2.5 Morphological methods

Morphological operations are based on mathematical theory and are techniques for the analysis and processing of geometrical structures and are most commonly applied to digital images. It provides a quantitative description based on measuring the changes in the binary image when it is subject to a particular transformation. (Michielsen & De Raedt, 2000)

2.2.6 Thresholding

Thresholding or segmentation is a form of image processing that allows distinction of pixels belonging to the feature of interest. Most grayscale images have

pixels that consist of values that range from 1 to 255. A thresholding value is chosen and any value less than it becomes zero and value greater than it becomes 255. This creates a binary image that consists solely of black or white pixels. (Soroushian & Elzafraney, 2005)

2.2.7 Two Point Correlation function

For a two-phase microstructure, a two point correlation function is the probability that a straight line of length l and angle theta is randomly placed on a 2d binary image of a microstructure and that both of its ends are contained in the particular phase of interest. Theta is the angle of the line between the x-axis of the xy coordinate system or the angle in a polar coordinate system. (Gokhale, Tewari, & Garmestani, 2005) It can be mathematically stated as :

$$S_2(r) = \frac{1}{2r+1}\sum_{i=0}^{2r} S_2\left(r, \frac{\pi l}{4r}\right) \quad 2.1$$

For isotropic media, $S_2(r)$ has a maximum value when $\lim_{r\to 0} S_2(r)$ which is equal to the pore area fraction. When $r\to\infty$ $S_2(r)$ approaches a horizontal asymptotic value. (HU, 2004) The behavior of region between r=0 and the asymptotic value corresponds to the state of dispersion of the pore phase. Perfectly random structures without any clustering effects will give a smoothly decreasing curve. The intersection of the slope of S_2 at (r)=0 and the horizontal asymptote give a characteristic value of the pore structure (l_{TPC}). This value can be used to define the average pore diameter d_{TPC} by use of the formula:

$$d_{TPC} = \frac{l_{TPC}}{(1-\phi_A)} \quad 2.2$$

(M. Sumanasooriya et al., 2010)

2.2.8 Granulometry

A granulometric analysis by a morphological opening is a general method that can be used independently of the nature of the image set. It is an approach to compute a size distribution of grains, phases, or pores in a binary image. A structuring element is used such as the diameter for a circular pore and these are used for opening the pixels of the region of interest (pore area) that are contained within the size of the structuring element. (Coster & Chermant, 2001) The pore area fraction after an opening operation can be plotted against the size of the structuring element. The normalized size distribution function is defined as:

$$N(k) = 1 - \frac{P_s(k)}{P_s(0)} \quad 2.3$$

where $P_s(k)$ is the sum of all the pixels in the image opened with kth structuring element, and $P_s(0)$ is the sum of all the pixels in the original images. A granulometric density function:

$$G(k) = N(k+1) - N(k) \quad 2.4$$

is basically a first derivative of the normalized size distribution function. A local maximum of this function correlates to the critical pore size d_{crit} for the corresponding structuring element. (Koleva et al., 2008)

2.2.9 Specific Surface Area and Mean Free Spacing

Specific surface area s_p is an important parameter the can be used to characterize a porous material. It is a measure of the total surface area of the pores per unit volume of

the material. It is necessary when using the Kozeny-Carmen equations for calculating permeability. (Berryman & Blair, 1986) Let S_p be the surface area of the pores and V be the total volume of the material. From the two-point correlation function it has been shown that:

$$\lim_{r\to 0} \frac{\partial S_2(r)}{\partial r} = -\frac{S_p}{4V} = -\frac{s_p}{4} \qquad 2.5$$

The mean free spacing of pores can be obtained using a stereological method or by a morphological operation such as the two-point correlation method. The variation of $S_2(r)$ between r=0 and the horizontal asymptote can describe the dispersion of the pore phases. The faster the asymptotic value is reached the closer the pores are together. For stereological purposes, the perimeter length of the pore features per unit area of the image (L_A) and the pore area fraction $\square_A$ are used to calculate the mean free spacing parameter λ. This parameter is defined as the average value of the surface to surface distances between all the neighboring pores. The mean free spacing parameter can be calculated as (M. Sumanasooriya & Neithalath, 2009)

$$\lambda = \frac{\pi(1-\phi A)\phi A}{L_A} \qquad 2.6$$

2.2.10 Pore Distribution density

The pore distribution density parameter contains details about the pore cluster size which implies the connectivity of the pores. The 2D distribution density can be calculated and then using stereological theory the 3D density parameter can be calculated. The 2D parameter (Γ_{2D}) can be found by using:

$$\Gamma_{2D} = \sum_{i=1}^{N} \frac{l_i^2}{A} \qquad 2.7$$

Where l_i is the length of the ith skeleton segment and N is the number of skeleton segments on an image of area A. The 3D parameter can calculated as follows: (Ye, Hu, Van Breugel, & Stroeven, 2002)

$$\Gamma_{3D} = \frac{32}{\pi^3}\Gamma_{2D} \quad 2.8$$

2.3 Tortuosity and Pore Connectivity

This section is on tortuosity (τ) and pore connectivity and how it pertains to porous media such as concrete. Tortuosity is a property of a curve being tortuous meaning it is twisted and having many terms. A common geometrical description of tortuosity is the ratio of the length to the curve to the distance between its ends. In terms of porous media, tortuosity is taken as the ratio of the average pore length L_e to the length of the porous medium along the major flow or diffusion axis. Tortuosity is defined then as L_e/L and since generally $L_e>L$, $\tau>1$ (Epstein, 1989a)

2.3.1 Measurement by diffusion coefficient

Due to the random drifting of particles in a fluid which is called Brownian motion, the average movement of molecules in terms of their mean-squre displacement is linearly proportional to time in bulk fluids. This motion is related to a proportionality constant which is called the bulk diffusion coefficient D_0. When fluid is confined in a porous medium such as pervious concrete, diffusion is restricted by the solid surfaces bounding the pore space. The diffusion coefficient is no longer a constant but rather a function of time.

$$D(t) = \frac{\langle r^2(t) \rangle}{6t} \quad 2.9$$

At short times D(t) is determined by the surface to volume ratio of the pore space and at long times it is determined by the toruosity or pore connectivity. Tortuosity may be defined as:

$$\frac{1}{\tau} = \frac{D_\infty}{D_o} \quad 2.10$$

where D_∞ is the steady state diffusion coefficient of fluid in a porous medium and D_0 is the diffusion coefficient of the fluid in free flow (Latour, Kleinberg, Mitra, & Sotak, 1995).

2.3.2 Linking hydraulic conductivity and tortuosity

The hyrdraulic conductivity or permeability of a porous media is by the arrangement and geometry of its pores and solids. Some statistical models for the permeability and hydraulic conductivity of porous media are only based on the distribution of pore sizes and only mimic the permeability of a bundle of straight capillary tubes. In reality it is much more complex, with twisted and crooked pores as some of them dead end while others are connected to other pores. This means there is a need to scale the permeability from the capillary tube model to include increased path length due to crookedness of the path (tortuosity). Pore connectivity and tortuosity are inversely related.

2.4 Permeability of Porous Media

Absolute permeability is defined as the measure of the ability of a porous material to transmit a single phase fluid. It is an intrinsic property of a material, independent of any external condition.

2.4.1 Kozenzy Carmen equation

The Kozeny-Carmen equation relates the permeability of the porous media to the average hydraulic radius of the pore space.

$$K = \frac{C_0 \tau \phi^3}{S^2} \qquad 2.11$$

The hydraulic radius is defined by the porosity (□) and the average pore perimeter (s). The equation also includes two matching parameters ; tortuosity (τ) and a pore shape factor C_0 (Vervoort & Cattle, 2003).

2.4.2 Katz-Thompson equation

Katz and Thompson used percolation concepts to derive an equation relating the permeability of saturated random porous media to microstructural descriptors and conductivities.

$$K = c\left(\frac{\sigma}{\sigma_0}\right)(l_c)^2 \qquad 2.12$$

The bulk and porewater conductivities are denoted as σ and σ_0 and and l_c is the crtical pore diameter and c is a constant on the order of 1/226. The equation was first applied to sandstone and sedimentary rock where the constant value of 1/226 was determined. (El-Dieb & Hooton, 1994)(Tumidajski & Lin, 1998). For pervious concretes specimens using aggregate sizes ranging from 4.5 to 12.5 mm, the constant of 1/(1.6*226) was found using experimental methods (Neithalath, Sumanasooriya, et al., 2010).

2.4.3 Lattice Boltzmann

The Lattice-Boltzmann method is a numerical scheme that is used in this study to simulate the permeability of enhanced porosity concrete. The following section explains the theory and its applications to EPC.

The Lattice Boltzmann method is an innovative numerical method based on the kinetic theory to simulate various hydrodynamic problems. Unlike conventional numerical schemes based on discretizations of macroscopic continuum equations, the Lattice Boltzmann method is based on microscopic models and kinetic equations. The basic premise for using these simplified kinetic-type methods for macroscopic fluid flows is that the overall macroscopic behavior of fluid flow is the result of the collective behavior of the many microscopic particles in the system. Also, the macroscopic dynamics of the fluid is not sensitive to the underlying physics of the microscopic particles. Even though the LBM is based on a particle model, its overall focus is the averaged macroscopic behavior.

The kinetic equation model provides many of the advantages of molecular dynamics, clear physical pictures, easy implementation of boundary conditions, and fully parallel algorithms. Since many of the fast computers today are of a massively parallel nature, the LBM can be easily implemented to take advantage of these abilities in a straightforward manner. The LBM is also highly attractive since its equations are linear and that the incompressible Navier Stokes equations can be obtained in the nearly incompressible limit of the LBM (Chen & Doolen, 1998).

The LBM approximates the continuous Boltzmann equation by discretizing a physical space with lattice nodes and velocity space on a set of microscopic velocity vectors. A lattice corresponds to a set of nodes that represents the discrete phase of physical space where each node corresponds to either a void or a solid.

Various models exist for numerical solutions of various fluid flow scenarios where each way has different way to characterize the particle interaction. The LB models are usually denoted as DxQy where x represents the number of demensions and y represents the degrees of freedom or velocity directions of each particle (Kutay, 2005).

The generalized form of the Boltzmann equation

$$\frac{\partial f}{\partial t} + u * \frac{\partial f}{\partial x} + F * \frac{\partial f}{\partial x} = \Omega(f) \quad 2.13$$

Where f is the distribution function, u is the velocity, Ω is the collision function, and F is the body force per unit mass. The distribution function, f, is a statistical function from which the macroscopic properties of the fluid can be found. The generalized Boltzmann equation is too complex and impractical to be solved directly for fluid simulations. (Kosuge, 2008) A discrete from of the equation is:

$$\frac{\partial f_i}{\partial t} + e_i * \frac{\partial f_i}{\partial x} + F * \frac{\partial f}{\partial x_i} = \Omega_i \quad 2.14$$

Where e_i is the directional velocity and f is the distribution function in the ith direction. After converting from Eulerian to Lagrangian coordinate systems and integrating, the equation becomes:

$$F(x + e_i, t + 1) = F_i(x, t) + \Omega_i - B_F \quad 2.15$$

Where the body forces are equal to:

$$B_F = -\frac{w_i}{c_s^2}(e_i * \nabla p) \quad 2.16$$

W_i is the weighting factor of the directional vector and c_s is the lattice speed of sound and ∇ p is the pressure gradiant. The collision function is expressed as:

$$\Omega_i = -\frac{F_i - F_i^{eq}}{\tau} \quad 2.17$$

Where τ is the relaxation factor and is function of the viscosity of the fluid. The equilibrium equation derived by He and Luo will work for the D2Q9 and D3Q19 models(He & Luo, 1997).

$$F_i^{eq} = w_i \rho \left[1 + \frac{e_i * u}{c_s^2} + \frac{(e_i * u)^2}{2c_s^4} - \frac{(u * u)}{2c_s^2}\right] \quad 2.18$$

The relaxation time τ can be related to viscosity as:

$$\nu = c_s^2 \left(\tau - \frac{1}{2}\right) \quad 2.19$$

The macroscopic velocity, u, and density, ρ can be calculated as:

$$\rho = \sum_{i=1}^{Q} F_i \quad 2.20$$

$$u = \frac{\sum_{i=1}^{Q} F_i e_i}{\rho} \quad 2.21$$

(Zhou, 2010)

2.4.4 Stokes Solver

To numerically estimate absolute permeability, the Stokes equations are solved:

$$\vec{\nabla}.\vec{V} = 0 \quad 2.22$$

$$\mu \nabla^2 \vec{V} - \vec{V} P = \vec{0} \quad 2.23$$

Where $\vec{\nabla}.$ is the divergence operator, $\vec{V}$ is the velocity of the fluid in the fluid phase of the material, μ is the dynamic viscosity of the flowing fluid, ∇^2 is the laplacian operator, and P is the pressure of the fluid in the fluid phase of the material. This equation system is a

simplification of the Navier-Stokes equations which considers the flow to be steady-state and laminar and the fluid is Newtonian and incompressible.

The boundary conditions include the fluid velocity vanishing at all fluid-solid interfaces and an applied pressure gradient across two of the faces comprising the three-dimensional microstructure. It is assumed that all pores in the three-dimensional microstructure are completely filled with fluid (saturated) (Bentz & Martys, 2007b).

2.5 Fracture mechanics Solid Concrete

The following section explains various methods to model the fracture behavior of concrete and porous media.

2.5.1 Nonlinear boundary element method

Concrete is a heterogeneous material consisting of coarse aggregate bound in a relatively soft mortar, which itself comprises fine aggregate, cement and water. During the setting up of the concrete, a large number of microcracks may develop, especially at the interface between coarser aggregate and mortar. Further microcracking may develop during the loading process because of the differences in the stiffness between and aggregate and mortar, resulting in a weak bond between them. It is generally understood that crack propagation in concrete structures is preceded by the formation of a thin but extended fracture zone. Material inside the fracture zone softens and behaves differently from the remaining part of the structure which is still assumed to be elastic. Therefore

the fracturing is nonlinear and must be modeled that way. The boundary element method is based on the transformation of the partial differential equation describing the behavior of the unknown inside, and on the boundary of the domain to a boundary integral equation relating only boundary values. Once the boundary integral equation is established, the numerical solution can be performed to solve this equation (Saleh, 1997).

2.5.2 Characterizing Elastoplastic Behavior

We can define an energy release rate for nonlinear elastic bodies, J, as the area on the load-displacement diagram between crack areas A and A+da. The critical value, J_{IC}, is the value of J corresponding to the total displacement at the onset of crack extension. J_{IC} is analogous to the critical stress concentration factor, K_{IC},for cracks in linear elastic solids. An alternative measure is the crack tip opening displacement (CTOD). In principle, the CTOD can be measured directly at the crack tip but in practice is usually inferred from crack mouth measurements (Sanford, 2003).

2.5.3 Static Fracture Testing Parameters

Three point bending beams with a central notch can be used for determining the static fracture parameters. The stress strength factor is determined based on an effective crack approach using principles of linear elastic fracture mechanics. The critical crack tip opening displacement $CTOD_c$ is determined using equation

$$CTOD_c = \frac{6F_{max}SaV_1(x)}{Eh^2B}[(1-\beta)^2 + (1.081 - 1.149\alpha)(\beta - \beta^2)]^{1/2} \quad 2.24$$

Where α=a/h, β=a_0/h and S, h and b represent the span, depth and specimen thickness, respectively, a_0 and Δa are the intitial notch length and increment crack growth. Also:

$$V_1(\alpha) = 0.76 - 2.28\alpha + 3.87\alpha^2 - 2.04\alpha^3 + \frac{0.66}{(1-\alpha)^2} \quad 2.25$$

Where $\alpha = \frac{a_0+\Delta a}{h}$. By measuring peak load at F_{MAX} and $a=a_0+\Delta a$ at successive intervals of crack growth, the stress intensity factor at the tip of the critical effective crack can be obtained by

$$K_{IC}^{e} = 3F_{MAX}\frac{S\sqrt{\pi a}F(\alpha)}{2h^2 b} \quad 2.26$$

in which

$$F(\alpha) = \frac{1.99-\alpha(1-\alpha)(2.15-3.93\alpha+2.7\alpha^2)}{\sqrt{\pi}(1+2\alpha)(1-\alpha)^{3/2}} \quad 2.27$$

(Deng, 2005)

2.5.4 Fracture Energy and Toughness

A toughness measurement that represents the energy absorbed by the specimen is computed from the area under the load-deflection response. This response is known to be influenced by specimen size and loading rate. Since it is preferable to obtain toughness as a material property independent of specimen and testing variables, or alternatively to minimize some of these effects, the ASTM 1018 procedure was used (ASTM C 1018-97, 1997). It involves determining the amount of energy required to deflect the beam a specified multiple of the first crack deflection.

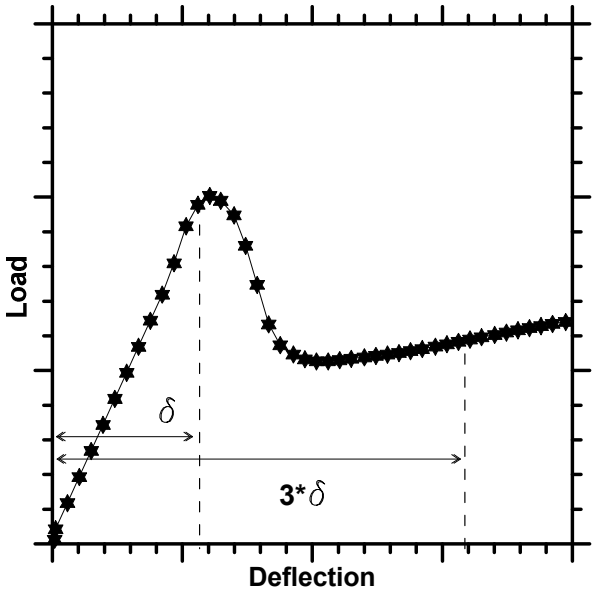

Figure 2-1 Important characteristics of the load-deflection curve

The toughness indices I_5, I_{10}, nd I_{20} are calculated as ratios of the area of the load deflection curve up to deflections of 3, 5.5, and 10.5 times the first crack deflection divided by the area up to the first crack deflection(Gopalaratnam et al., 1991). These indices provide an indication of the relative toughness at these deflections.

When a concrete structure with a quasi brittle crack is subjected to loading, the applied load results in an energy release rate G_f at the tip of the of the effective crack. G_f is the energy release rate for propagation of a unit length of a crack in a structure with unit thickness and is regarded as a material fracture parameter. This value is found by using the following equation:

$$G_f = \frac{W_t}{(b-a_0)t} \qquad 2.28$$

Where W_t is the total area under the load displacement curve, b is the total depth of the beam, t is the thickness of the beam and a_0 is the depth of the notch (Shah et al., 1995).

2.6 Summary

This chapter has provided a concise review of some of the relevant literature in the areas of general aspects of, 2D pore structure analysis, permeability, and fracture behavior of porous media. This literature review has served as the basis in defining the scope of this research work.

3 CHAPTER 3: MATERIALS/TEST METHODS

3.1 General

This chapter describes the different materials used in the research along with the test methods and procedures employed to study the various properties of pervious concretes. The testing techniques that were adopted to study the properties of pervious concretes were based on accepted standards.

3.2 Materials and Mixtures

The pervious concrete mixtures were prepared using Type I/II Ordinary Portland Cement (OPC) and limestone coarse aggregates. In general, pervious concretes are proportioned using gap-graded aggregates. The most common aggregate sizes used are #4 or 4.75 mm (passing 9.5 mm, retained on 4.75 mm sieve), or 3/8" or 9.5 mm (passing 12.5 mm, retained on 9.5 mm sieve) (Marolf et al., 2004)(Omkar Deo & Neithalath, 2011)(Neithalath et al., 2006), which have been adopted in this study also. Maintaining a large open porosity necessitates a low water-to-cement ratio (w/c of 0.30 is used in this study) and the absence of fine aggregates. Pervious concrete mixtures using both of the above mentioned aggregate sizes were designed to achieve two different levels of porosity: 19% and 25%. For a few mixtures, monofilament/fibrillated polypropylene fibers were incorporated at 0.5% or 1.0% by volume of the mixture. Beyond a fiber volume of 1.0%, it was difficult to homogenize the mixture. The fibers were 54 mm long, and had a specific gravity of 0.91. A total of 12 different pervious concrete mixtures were thus proportioned, having different pore structure features. A mixture proportioning methodology based on granular particle packing method was employed to obtain the desired porosities. Extensive details on the formulation of the proportioning method can

be found in (Milani S. Sumanasooriya et al., 2012)(Okar Deo, 2010). The virtual packing densities of the components of the mixture, the actual packing density of the mixture, and the corresponding volume fractions are used to determine a compaction index, which in turn is related to the material porosity. The fresh porosity of the samples were determined in accordance with ASTM C1688 (ASTM C1688/C1688M-13, 2009). The fresh concrete mixtures were cast in rectangular beams 100 mm x 100 mm in cross section and 400 mm long for fracture studies, and 100 mm diameter x 200 mm long cylinders for compressive strength testing and image analysis for pore structure feature determination. The casting and compacting sequence for the beams and the cylinders to achieve the desired porosities were arrived at based on trial batches. A conventional concrete mixture (cement content of 400 kg/m^3 and w/c of 0.42) was also proportioned to facilitate comparison. A total of 36 pervious concrete beams and 72 cylinders were cast. They were demolded after 24 hours of curing in the molds and then moist-cured for 28 days in a curing chamber (> 98% RH) before the respective tests were carried out. For the beam specimens, 20±1 mm deep notches were cut at the mid-span for fracture tests.

3.3 Determination of Porosity and Pore Sizes

Details of determining the overall porosity and pore sizes of the pervious concretes are described in the following section.

3.3.1 Volumetric porosity measurements

The porosity of the hardened specimens was experimentally measured by using a method that determines the volume of water displaced by a fully submerged cylindrical specimen. 25 mm thick slices were cut off from the top and bottom of the cylindrical specimens, and they were allowed to air dry overnight. The specimens were submerged in a tank of water while placed in a metal cage connected to a scale. The mass of the specimen in air and in water (w_{air} and w_{water}) and the specimen volume ($V_{specimen}$) was measured and the volumetric porosity (ϕ_v) determined as:

$$\phi_v = 1 - \left[\frac{(w_{air} - w_{water}) / \rho_{water}}{V_{specimen}} \right] \quad 3.1$$

3.3.2 Image analysis for area fraction of porosity, pore sizes, and mean free spacing

The cylindrical specimens which were used for volumetric porosity measurements were also used to obtain planar images for the determination of different pore structure features. The cylindrical specimens, after removing the ends, were cut into three equal parts by sectioning at approximately 42 mm thick intervals. At least six planar faces were thus available from a single cylindrical specimen to be subjected to image analysis to obtain the pore structure features. Two specimens were used to obtain the planar images for the analysis of pore structure features. To measure the area fraction of pores (ϕ_A), planar sections of pervious concrete specimens were polished to obtain smooth surfaces and scanned using a flatbed scanner in the grayscale mode at a resolution of 300 dpi. Five to eight good images were obtained corresponding to each mixture for feature analysis

after neglecting the ones that exhibited significant edge effects. The scanned images were cropped into circular images having a diameter of 570 pixels, and were thresholded to separate the pore and solid phases. The images were further processed to remove noise and then cropped into 400 pixel (66.7 mm) square images. Image J® software was used for image processing and analysis. Further explanation of the steps in image processing and analysis can be found in (Omkar Deo & Neithalath, 2010)(Neithalath, Bentz, et al., 2010)(M. Sumanasooriya et al., 2010). The area fraction of the pores in the binary image was calculated for all the planar sections of each specimen, and the average value reported as ϕ_A.

The pore sizes of the pervious concrete specimens were determined using Two-Point Correlation (TPC) functions (Torquato, 2001) as well as a granulometric operation. The TPC function can be obtained by randomly throwing line segments of length "*l*" with a specific orientation into a two-dimensional image of a two-phase material and counting the fraction of times both end points of the line lie in the phase of interest (Torquato, 2001). Figure 3-1(a) shows a typical TPC function ($S_2(l)$) for the planar image shown in the inset. The value of the TPC function at l=0 provides the porosity of the image. The correlation length (l_{TPC}), which is defined as the abscissa of the intersection point of the slope of TPC function at l = 0 and the horizontal asymptote at which $l \to \infty$, provides an estimate of the pore diameter (d_{TPC}) as:

$$d_{TPC} = \frac{l_{TPC}}{1-\phi_A} \qquad 3.2$$

ϕ_A is the pore area fraction of the image, which corresponds to the value of the TPC function at l = 0. Granulometric distribution function is a morphological opening distribution function that can be used to characterize the feature size distribution in a two-dimensional image (Neithalath, Bentz, et al., 2010)(Coster & Chermant, 2001). The method consists of applying morphological opening with structuring elements (SE) of increasing size. For each opening, the pore area fraction of the image is computed by considering the sum of the pixel values in the opened image and in the original image. The diameter of the SE corresponding to the local maximum in the derivative function relates to a characteristic pore size of the material (d_{crit}), as shown in Figure 3-1(b).

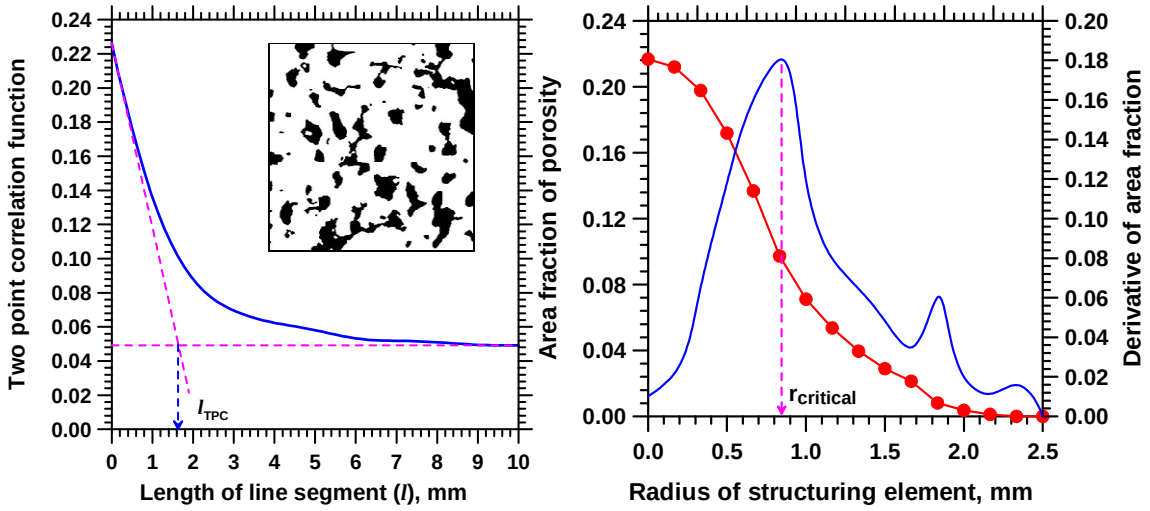

Figure 3-1:(a) Two-point correlation function (in the inset, a two-dimensional image used for TPC generation), and (b) granulometric opening function of a planar image to determine the pore size

Mean free spacing (λ) is defined as the average value of uninterrupted surface-to-surface distances between all the neighboring pores in three dimensions. The mean free spacing can be considered to influence the mechanical properties such as the strength and

fracture behavior, and can be related to the pore area fraction (ϕ_A), and the perimeter length of the pore features per unit area of the image (L_A) using Equation 2 that is based on stereology:

$$\lambda = \frac{\pi(1-\phi_A)\phi_A}{L_A} \quad 3.3$$

where ϕ_A and L_A were extracted from planar images of pervious concrete specimens.

3.4 3-D Reconstruction and Overall 3DTortuosity

Two-dimensional images (400 pixel square, Section 2.2.2) were used along with a correlation filter based three-dimensional reconstruction algorithm (M. Sumanasooriya & Neithalath, 2009)(M. Sumanasooriya et al., 2010)(Bentz, 2008) to generate three-dimensional pervious concrete structures. This algorithm along with the TPC function (Figure 1(a)) was used to reconstruct 300 voxel x 300 voxel x 300 voxel digitized three-dimensional material structures having similar volumetric porosity (ϕ_V), pore surface area, and correlation function as that of the real pervious concrete specimens (Figure 3-2(a)). The hydraulic radii (ratio of the cross-sectional area of the pore to its perimeter, or the ratio of total pore volume to the total surface area of pores) of these reconstructed structures were found to be lower than those of the original two-dimensional images used for reconstruction. Hence, a sintering algorithm (Bentz & Martys, 1994) was used to modify the reconstructed structures in order to bring their hydraulic radii closer to that of the parent image. The computer programs used for the reconstruction and the detailed procedure are elaborated in (M. Sumanasooriya et al., 2010)(Bentz & Martys, 2007a)(Garboczi, Bentz, & Martys, 1999).

The reconstructed 3-D structures were used to determine the tortuosity of the pore structure of pervious concretes. A watershed algorithm implemented in AvizoFire™ was used to accomplish this objective (Mangan & Whitaker, 1999)(Bieniek & Moga, 2000). Connected components were created through segmentation of the 300 images that made up the 3D system. Any pore that has a minimum size of 10 pixels that is connected to another pore in an adjacent image is labeled. A porosity analysis wizard in AvizoFire™ was then used which first reduces any noise and then detects the main voids from the labeled connected pores. It then separates the connected voids as individual objects that have a separation criterion of 300 voxels. A quantification tool was then implemented to calculate the tortuosity, which calculates the average lengths between the connected pores through the depth of the image and divides it by the image depth. Figure 3-2(b) shows the interconnected pore system where the pore network is made transparent, and Figure 3-2(c) shows a view of the internal structure. While the pores appear disconnected in 2D, they are completely connected in 3D as evidenced by the high values of computational permeability of the reconstructed structures (M. Sumanasooriya et al., 2010)(Bentz, 2008).

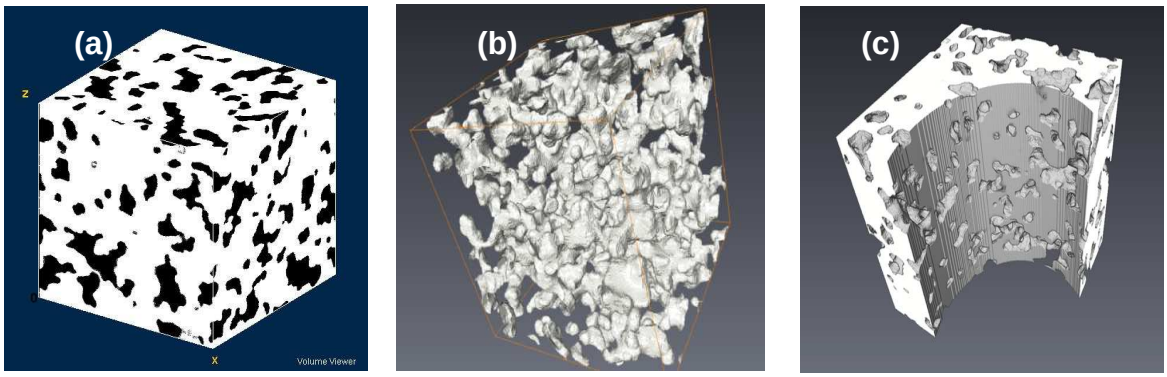

Figure 3-2: (a) 3D reconstructed structure of pervious concrete made using #4 aggregates and having a 25% porosity, (b) the pore network (in bright color), and (c) a view of the internal structure

3.5 Determination of Strength and Fracture Parameters

The compressive strengths for various pervious concrete specimens were determined using a 110 kip (490 kN) closed-loop universal testing machine operating in displacement controlled mode. The specimen ends were ground in a grinding machine and polished to ensure a smooth surface. Neoprene-rubber pads were used at the specimen ends for compression testing. A strain rate of 100 με/s was used and the stress-strain response recorded, from which the peak strength was obtained.

The fracture response of pervious concrete specimens was characterized using the two-parameter fracture model (Y. Jenq & Shah, 1985)(Y. S. Jenq & Shah, 1985)(Shah et al., 1995)(Bazant, 2002). The material fracture parameters - the critical stress intensity factor (K_{IC}), and the critical crack tip opening displacement ($CTOD_c$), were determined using three-point bend tests on notched beams, as shown in Figure 3(a). While the test method based on the two-parameter model suggests a notch depth equal to one-third of the beam depth, the value used in this study was one-fifth, because the large porosity in the material coupled with a higher initial notch depth resulted in instabilities in the measured crack mouth opening displacements (CMOD). The fracture tests were carried out on a closed loop testing machine with the CMOD, measured using a clip gage, as the feedback signal. Since it was experimentally difficult to initiate unloading at 95% of the

peak load as suggested in (Shah et al., 1995), (moreover, the random heterogeneous nature of the material results in strength variations between specimens of the same proportions) a modified procedure that eliminates the operator control of unloading (Jansen, Weiss, & Schleuchardt, 2000), and uses a CMOD of 0.5 mm as a preset point of unloading was used. The procedure to calculate K_{IC} and $CTOD_c$ from the experimental load-CMOD relationships, including the modified method (the focal point method) has been reported elsewhere (Y. Jenq & Shah, 1985)(Y. S. Jenq & Shah, 1985)(Shah et al., 1995)(Jansen et al., 2000). The focal point method allows extending the two-parameter fracture model to provide relationships between crack extension and the resistance to crack extension, as will be shown later in the paper. The two-parameter fracture model involves the use of the peak load, loading and unloading compliances, the specimen and notch geometry, and appropriate geometry correction factors. The geometry correction factors depend on the ratio of notch depth (a) to the beam depth (d) and can be found in (Shah et al., 1995). Figure 3-3(b) shows the focal point method (Jansen et al., 2000) used to determine the compliances used in the calculation of K_{IC} and $CTOD_c$. The loading compliance (C_i) was calculated as the inverse of the slope from 10% until 60% of the peak load. The unloading compliance was taken as the inverse of the slope of the unloading curve at the point of maximum convexity. This value provided a reasonably close approximation of the averages of the compliances when the slopes at the beginning of unloading or where the unloading curve meets the CMOD axis were considered. The differences between all the three different unloading compliances were not more than 5%.

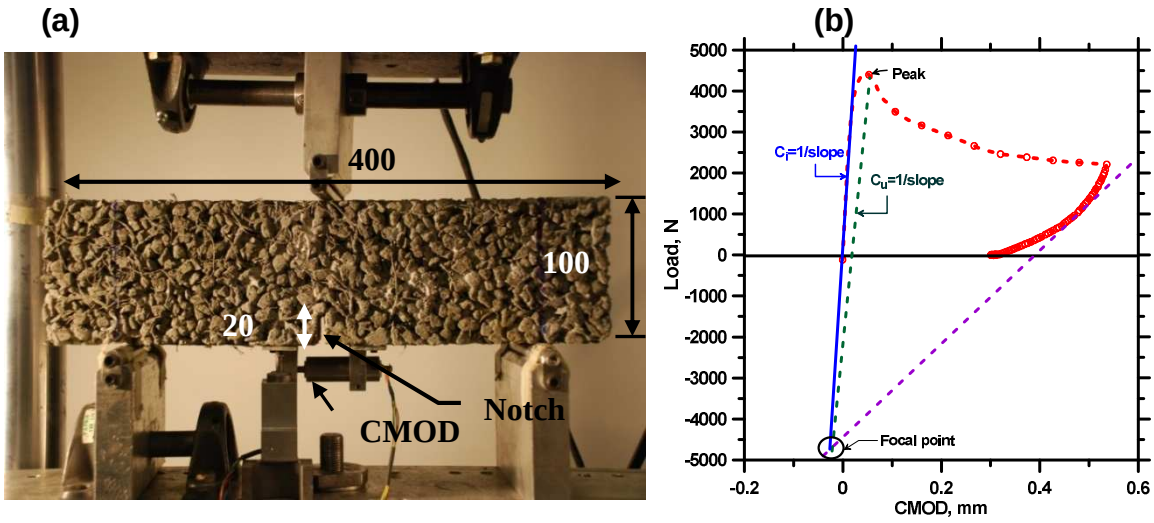

Figure 3-3: (a) Experimental set up for fracture tests based on the two-parameter fracture model, and (b) a typical load-CMOD plot and determination of the loading and unloading compliances (based on (Jansen et al., 2000))

3.6 Summary

This chapter has provided the test methods and procedures for determining the pore structure features and porosity of pervious concretes. The methods for creating 3D reconstructions and determining tortuosity were also explained. The test method for determining the mechanical and fracture behaviors of pervious concretes were described as well.

4 CHAPTER 4: PERMEABILITY AND TORTUOSITY

4.1 General

The permeability properties and tortuosity factors of various pervious concrete specimens as well as several geometric pores of specific designs were studied in this research and are presented in this chapter. A properly designed and implemented porous pavement system allows for polluted water to pass through the pavement into an infiltration bed, store the water temporarily if necessary in the gravel sub-base and then into the natural ground where by then much of the pollutants have been removed. It is important to study the characteristics and features of pervious concrete that allow the flow and penetration of water. Previous studies (Haselbach et al., 2006)(Neithalath, Sumanasooriya, et al., 2010)(Bentz, 2008) have conducted permeability calculations on pervious concrete. The tortuosity of pervious concretes have been studied (Epstein, 1989b)(Latour et al., 1995).

4.1.1 Lattice Boltzmann method

The Lattice Boltzmann method is an innovative numerical method based on the kinetic theory to simulate various hydrodynamic problems. Unlike conventional numerical schemes based on discretizations of macroscopic continuum equations, the Lattice Boltzmann method is based on microscopic models and kinetic equations. The basic premise for using these simplified kinetic-type methods for macroscopic fluid flows is that the overall macroscopic behavior of fluid flow is the result of the collective

behavior of the many microscopic particles in the system. Also, the macroscopic dynamics of the fluid is not sensitive to the underlying physics of the microscopic particles. Even though the LBM is based on a particle model, its overall focus is the averaged macroscopic behavior.

The kinetic equation model provides many of the advantages of molecular dynamics, clear physical pictures, easy implementation of boundary conditions, and fully parallel algorithms. Since many of the fast computers today are of a massively parallel nature, the LBM can be easily implemented to take advantage of these abilities in a straightforward manner. The LBM is also highly attractive since its equations are linear and that the incompressible Navier Stokes equations can be obtained in the nearly incompressible limit of the LBM. (Chen & Doolen, 1998)

The LBM approximates the continuous Boltzmann equation by discretizing a physical space with lattice nodes and velocity space on a set of microscopic velocity vectors. A lattice corresponds to a set of nodes that represents the discrete phase of physical space where each node corresponds to either a void or a solid (Kutay, 2005).

4.1.2 Katz-Thompson

According to the Katz-Thompson theory an expression for the permeability coefficient, k, can be expressed in terms of pore structure parameters and is given in the following way:

$$k = c * {d_c}^2 \left(\frac{\sigma}{\sigma_0}\right) \qquad 4.1$$

Where, d_c is the characteristic pore diameter that dominates fluid transport and can either be l_{tpc} from the two-point correlation function or the critical pore diameter from granulometry. Sigma (σ) is the conductivity of the porous material saturated with brine solution of electrical conductivity σ_0. C is a dimensionless parameter that takes into account all the tortuosity and connectivity of the pore network and is usually on the order of 1/226.

The critical pore diameter was defined as the smallest pore diameter in which a connected path could form from one side of the sample to the other. The Katz-Thompson equation was validated experimentally with a mercury intrusion apparatus. The rapid rise in the curve of the intruded pore volume versus pore radius was interpreted to occur when the mercury initially formed a connected pathway through the entire sample. Then by measuring the electrical resistance of the sample, it was proven to show the inflection point corresponded to the threshold for electrical continuity throughout the sample(El-Dieb & Hooton, 1994).

4.1.3 Stokes Solver

The permeability k is defined by the darcy relation:

$$v = \left(\frac{k}{\eta}\right) \nabla p \qquad 4.2$$

where v is the velocity of the fluid through the porous material, η is the viscosity of the fluid,and ∇p is the pressure gradient imposed across the specimen.

Software freely available from ftp://ftp.nist.gov was used to predict the electrical conductivity $\left(\frac{\sigma}{\sigma_0}\right)$ and the permeability k from the reconstructed 3d virtual specimens. The software for this program accepts as input a 3-d digital image, converting it into a real conductor network. The conjugate gradient method is used to solve this finite difference representation of Laplace's equation for real conductivity problems. Periodic boundary conditions are maintained. The permeability was computed by numerically solving the Navier-Stokes equations under incompressible stokes flow conditions.

4.1.4 Tortuosity

Tortuosity (τ) is defined as the ratio of the longest path traveled by the fluid particles

(L_e) to the shortest distance between two ends of a specimen (L):

$$\tau = \frac{L_e}{L} \qquad 4.3$$

In a 3D pore space, there are various possible paths that fluid can travel. A set of Matlab programs developed by Dr. Muhammed Kutay were used to determine the tortuosities of the reconstructed pervious concrete specimens. These values were estimated as follows: after obtaining the interconnected pore structure using a pore connectivity algorithm, isolated pore cross sections were grouped in each image slice and the centroid of each group was connected to the centroid of the closest pore cross sectional area in the next image slice. For each line connecting two pore cross sections, a tortuosity was calculated

by dividing the length of the connecting line to the vertical distance between two slices(Kutay, 2005).

There was a mistake in the way the code was originally written. The arrays were not being completely reset for each iteration. For example, if there were 8 centroids in one image and only 7 in the next image, the eighth value would still be carried through until it reached an image that had 8 centroids again. These extra values would create a straight vertical pore that would significantly lower the average tortuosity value.

4.2 Reconstructions

Pervious concrete reconstructions of 19, 22 and 27% porosities and with aggregate sizes of 3/8" and #4 were used in permeability and tortuosity simulations. Various geometric shapes were also created using Matlab and they had their tortuosities and permeabilities were calculated in the same manner as described above. A straight, S-shaped, branching and two zigzag patterns were created with two different porosities of 10 and 20%. Figure 4-1

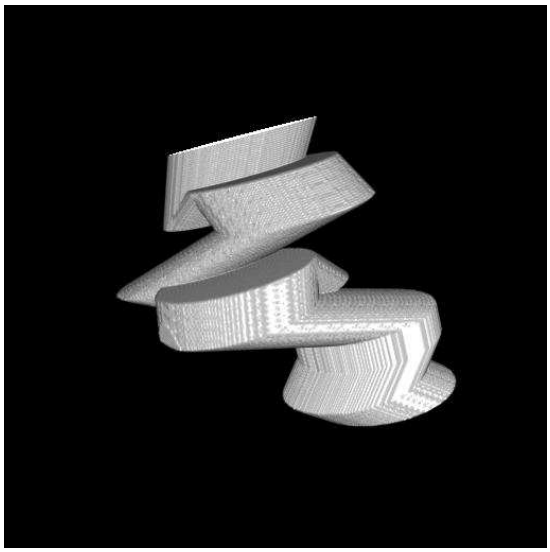

Figure 4-1 Ideal Geometric Zig-Zag Pattern

In Figure 4-1 Ideal Geometric Zig-Zag Pattern a zigzag pattern with an overall porosity of 20% can be seen. The diameter of the pore is 152 pixels. The image is 300 pixels in depth as all other reconstructions were done in this manner.

The term beta comes from dividing the electrical conductivity $\left(\frac{\sigma}{\sigma_0}\right)$ by the porosity (□) of the specimen. The inverse of beta will give an equivalence of the tortuosity of the specimen as well(Vervoort & Cattle, 2003). In the figure below, the tortuosity calculated from the matlab codes and the beta term determined from the NIST software can be seen for the ideal geometrically shaped specimens. The figure shows two different porosities with three different pore sizes. Since tortuosity is an inverse of the beta term, the data should follow a hyperbolic trend which is what is seen in the figure. This shows that the electrical conductivity algorithm is in agreement with the tortuosity which is verifiable since they are geometrically ideal shapes

4.3 Comparisons and Analysis

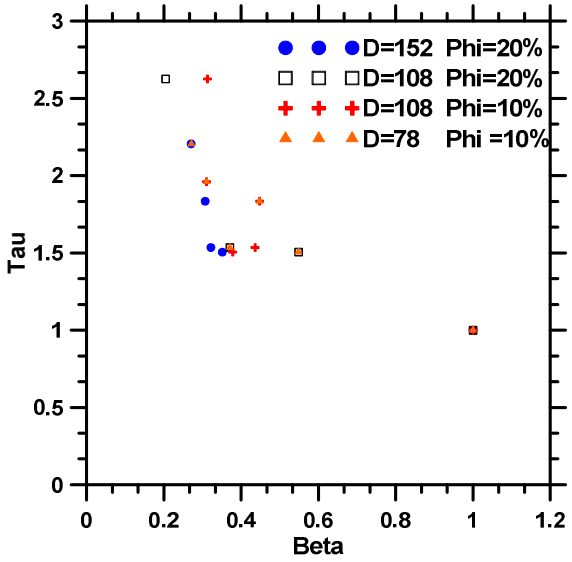

Figure 4-2 Tortuosity vs beta for ideal geometric shapes

The Katz-Thompson equation and the Stokes solver simulations are in relatively good agreement with one another for the ideal geometric shapes. There is two different porosities and three different pore diameters. In Figure 4-3the Stokes values are slightly higher than the Katz-Thompson values and are probably due to the fact the constant value of 1/226 was found experimentally when using sandstone and other porous kinds of rock and not pervious concrete. In Figure 4-4 the permeabilities calculated by the Katz-Thompson equation and by the Stokes solver for pervious concrete specimens are shown. Again there is a larger value determined using the Stokes solver and is more than likely due to the constant value of the Katz-Thompson equation.

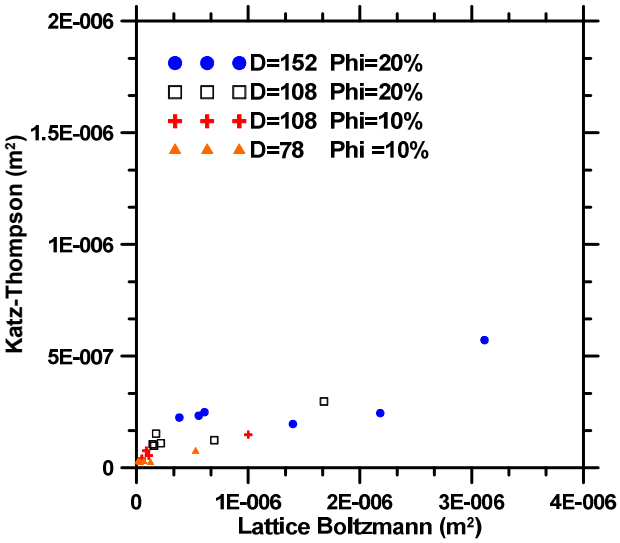

Figure 4-3 Permeability values of ideal geometric shapes determined by Katz-Thompson vs. Stokes solver

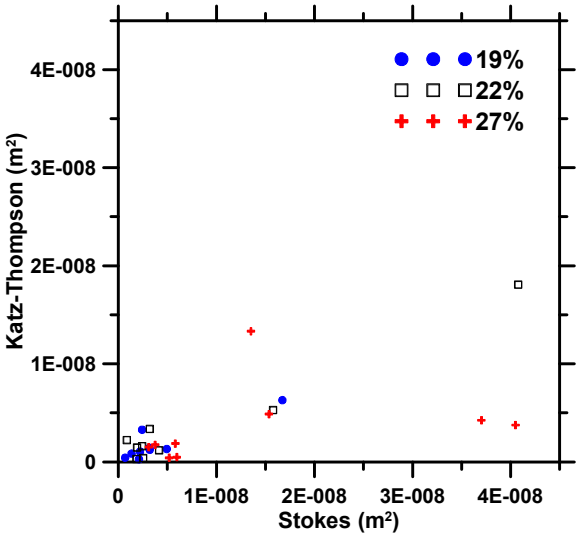

Figure 4-4 Permeability values of pervious concrete determined by Katz-Thompson vs. Stokes solver

The Stokes solver and the Lattice-Boltzman method are in almost a one to one ratio for the porous concrete reconstructions of 19, 22, and 27% porosities. These values can be

seen below in Figure 4-5. This shows that the two different methods of numerically determining permeability are relatively accurate.

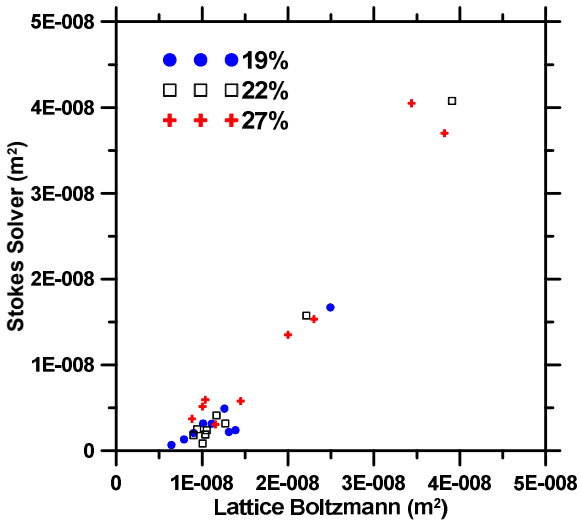

Figure 4-5 Permeability values of pervious conccrete determined by Stokes solver vs. Lattice Boltzmann method

4.4 Permeability simulations of human teeth

The permeabilities of human teeth were studied as the porosity of the internal material is similar to that of pervious concrete and there are many further studies in regards to dental procedures that would need to understand this phenomenon. Real tooth samples were not used but rather 3d reconstructions were created from actual 2d images.

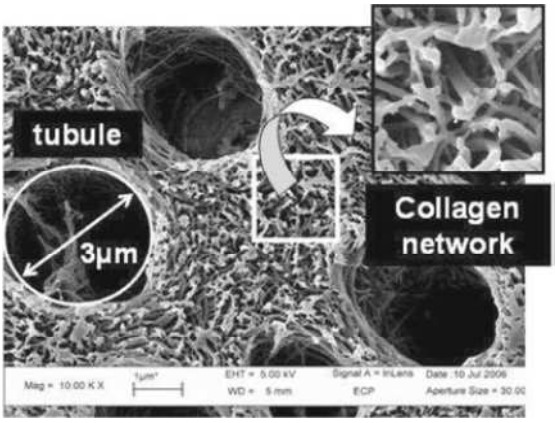

Figure 4-6 and Figure 4-7 were taken from “Collagen Fiber Network Infiltration: Permeability and Capillary Infiltration” by Vennat et al. The image from figure 2 was rendered using Fiji software. The image was first cropped so it only contained 400x400 pixels. Then it was thresholded to a level of 88 which achieved an approximate porosity of 55%. The noise was then reduced as well and the binary image was then saved as a jpg file.

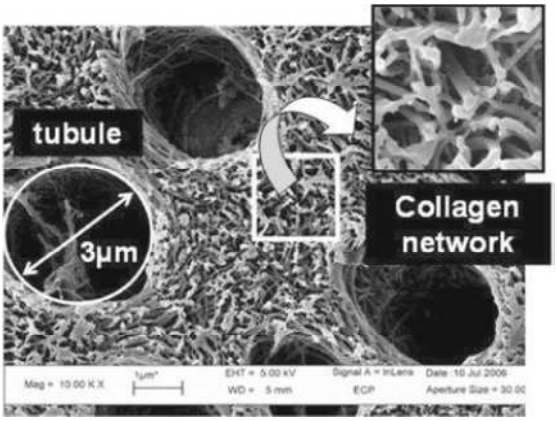

Figure 4-6 Original Image showing Collagen Network

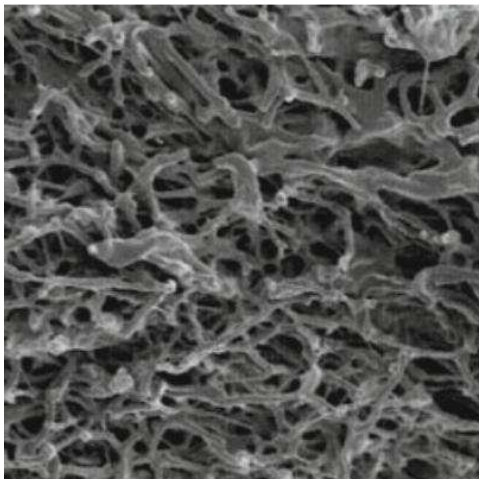

Figure 4-7 Image Used to Reconstruct 3D Model

The same 3d reconstruction algorithm that was used with pervious concrete specimens was used to generate a 3d image based on the binary 2d image which can be seen in figure 3. These 3d images were 300x300x300 pixels in size. A Matlab code was used to generate holes that transcended the entire cube in the z-direction. Three holes were first created that had constant diameter of 3 micrometers. Then 3 holes were created that began with a diameter of 3 micrometers and tapered linearly to a diameter of 2.25 micrometers. Finally, 3 holes were created that had a constant diameter of 3 micrometers but curved throughout the cube in an S shape manner.

The permeability was then found using the Stokes permeability solver algorithm and the Lattice-Boltzmann method. The 3d images were reduced to 200x200x200 pixels to save on computation time when using the Lattice-Boltzmann code.

Figure 4-8 is the 3D reconstructed model without any holes added and it has a scale of 112 pixels per micrometer. Its porosity is equal to 0.557. The journal article by E. Vennet gives a porosity for the collagen matrix of 0.55 and empirical values of permeability that range from 10e-16 m^2 to 10e-18 m^2 (Vennat, Aubry, & Degrange, 2010).

Figure 4-9 is the reconstructed 3d image with holes added that have a constant diameter of 3 micrometers. Figure 4-10 is the reconstructed 3d image with 3 tapered holes added to the model. The holes begin with a diameter of 3 micrometers and decrease linearly to a diameter of 2.25 micrometers. Figure 6 is the reconstructed 3d image with S shaped holes that have a constant diameter of 3 micrometers. The scaling factor is 38 pixels per micrometer for Figure 4-8,Figure 4-9,Figure 4-10.

An image of human enamel can be seen in Figure 4-11 (Poole, Newman, & Dibdin, 1981). A 400x400 pixel image was extracted using Fiji image analysis software and it was thresholded to a value of which gave an overall porosity of 0.027. The average porosity of human tooth enamel was found to range from 0.018 to 0.038.(1) The average thickness of human tooth enamel relative to human dentin is known to be approximately 8% of the total dentin and enamel layers combined (Olejniczak et al., 2008).

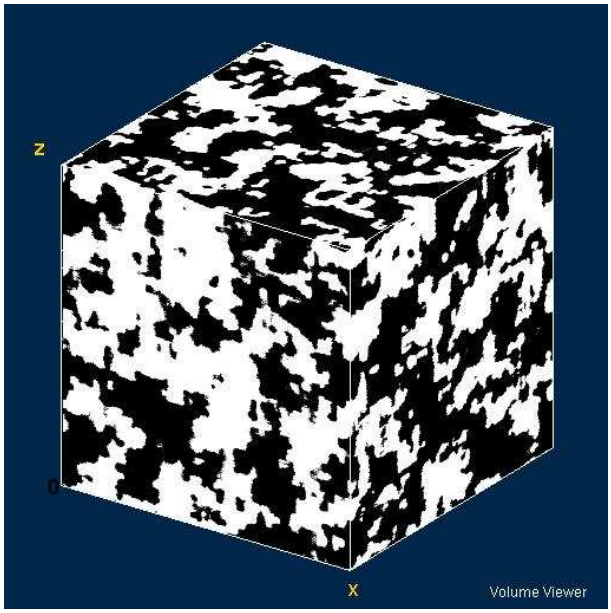

Figure 4-8 Reconstructed 3D Model of Pure Collagen

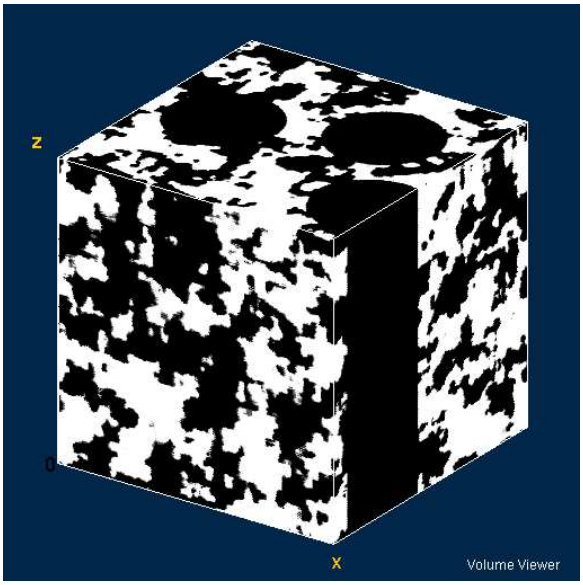

Figure 4-9 Reconstructed 3d model with 3 micron straight holes

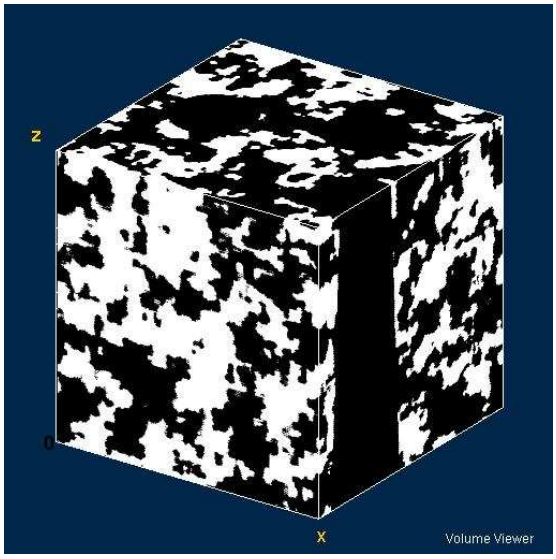

Figure 4-10 Reconstructed 3D Model with 3 Micron Tapered Holes

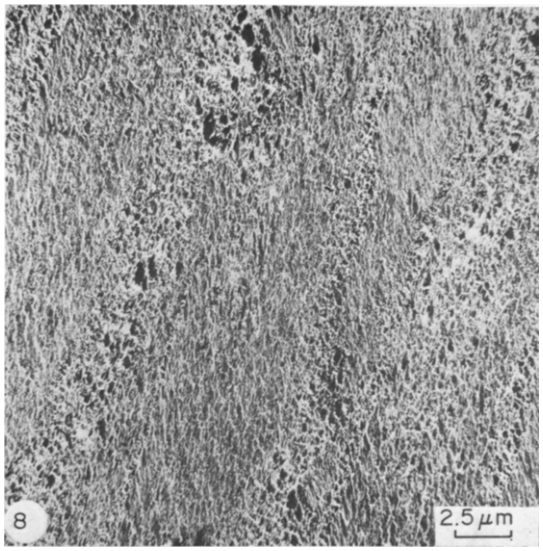

Figure 4-11 SEM of human tooth enamel

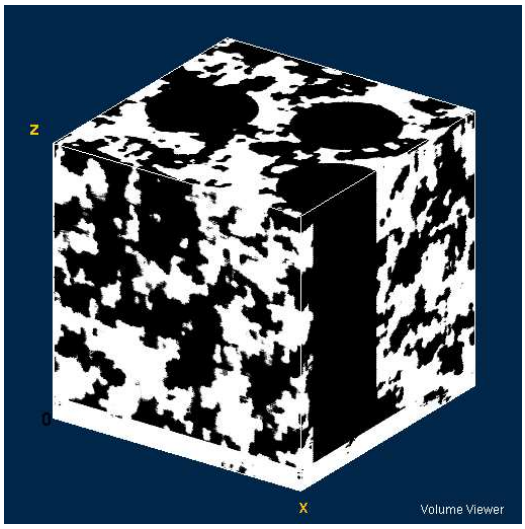

Figure 4-12 Reconstruction with straight holes with a layer of enamel

A 3d image of the tooth enamel was constructed using the same software that was used for the dentin image. Then using Fiji software, the enamel images were stacked with the collagen images containing the straight 3 micron diameter pores to create a composite image which can be seen in Figure 4-12. The composite 3d image contains 8% enamel and the rest is dentin collagen. 24 enamel images were stacked on top of 276 collagen images. The scaling factor is 38 pixels per micrometer. A second composite image was created where the enamel was twice the thickness as before which consisted of 48 enamel images and 252 collagen images. The permeabilities were calculated using the Stokes Solver and the Lattice Boltzmann method for both of the composite images as well for an entire 3d cube of pure enamel.

Table 4-1 consists of all the permeability calculations and all of the units are in meters^2. These values are in relatively good agreement with the actual empirical values that range from 10e-16 m^2 to 10e-18 m^2.

Table 4-1 Permeability results from Stokes solver and Lattice Boltzmann method, values are in m2

	Pure collegen	**Straight holes**	**Tapered holes**	**S shaped holes**	**Pure enamel**	**Composite de 1**	**Composite de 2**
Stokes Solver	2.799E-16	3.246E-14	2.299E-14	1.461E-14	8.483E-22	4.722E-18	5.796E-19
Lattice Boltzmann	1.259E-16	1.172E-15	5.665E-16	5.984E-16	N/A	8.745E-17	8.772E-17

4.5 Summary

This chapter has focused on studying the relationship between permeability and tortuosity as it pertains to porosity and pore size of pervious concrete. Various ideal geometric shapes were also constructed that had varying pore sizes and porosities. The pervious concretes also had differing pore sizes and porosities. The permeabilities were determined using three different methods; Stokes solver, Lattice Boltzmann method and the Katz-Thompson equation. These values were then compared to the tortuosity values determined using a Matlab code that uses a pore connectivity algorithm. The tortuosity was also determined from the inverse of the conductivity determined from a numerical analysis that was necessary for using the Katz-Thompson equation. These tortuosity values were then compared to the permeabilities. The pervious concretes and ideal geometric shapes showed consistent similarities between the tortuosities and the permeabilities.

Reconstruction of human teeth from actual SEM images of dentin and enamel were created and the permeabilities were determined using the Stokes solver and Lattice Boltzmann method. These values were found to be consistent with empirical values found in literature.

5 CHAPTER 5: FACTURE TOUGHNESS

5.1 General

This chapter describes the fracture response of pervious concrete specimens proportioned for different porosities as a function of the pore structure features and fiber volume fraction. Stereological and morphological methods are used to extract the relevant pore structure features of pervious concretes from planar images. A two-parameter fracture model is used to obtain the fracture toughness (K_{IC}) and critical crack tip opening displacement ($CTOD_c$) from load-crack mouth opening displacement (CMOD) data of notched beams under three-point bending. . A sensitivity analysis also is employed to quantify the influence of material design parameters on $K_{IC.}$

5.2 Pore Structure Features: Porosity, Pore Sizes, and Tortuosity

The porosity and pore sizes of the chosen mixtures were determined as explained in Section 2.2. Volumetric porosity was determined on cylindrical specimens while planar area fraction of pores was determined directly from the images as well as through the implementation of TPC functions to the images. Figure 5-1(a) and (b) depict the porosities of the specimens made using #4 and 3/8” aggregates determined using all the methods mentioned above, which are found to be very comparable to each other, and closer to the design values of 19% and 25%. Therefore volumetric porosity will be used

as the measure of the pore volume in the remainder of this paper since it is one of the easiest pore structure features to quantify. Figure 5-2 shows a comparison of pore diameters determined using the TPC and granulometric distribution functions for all the specimens studied. A general trend of increasing pore sizes with increasing aggregate sizes can be observed, with no real dependence of pore sizes on porosity when similar size aggregates are used (M. Sumanasooriya & Neithalath, 2009)(Neithalath, Bentz, et al., 2010).

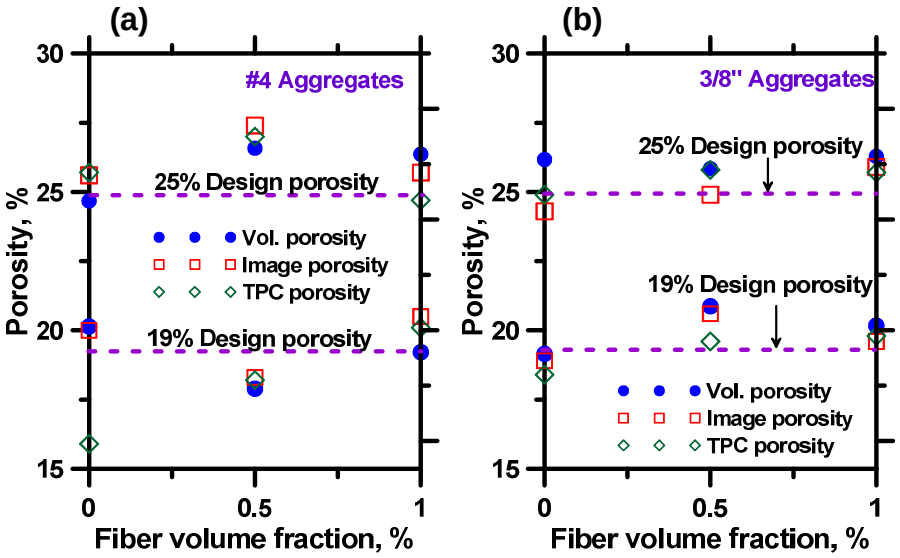

Figure 5-1: Porosities of the pervious concrete specimens made using: (a) #4 aggregates, and (b) 3/8” aggregates

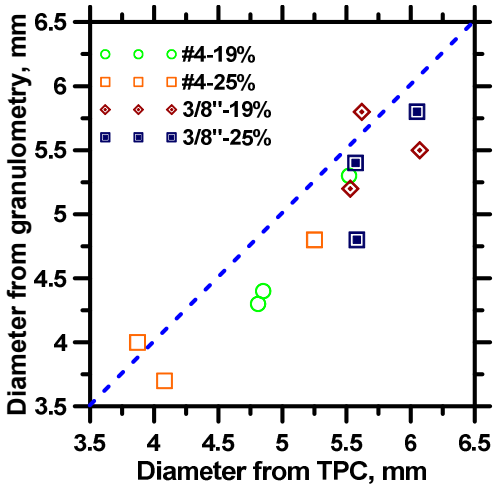

Figure 5-2: Comparison of pore sizes of pervious concretes determined using different methods

In order to assess the statistical similarity of pore structure features (porosity and pore sizes) determined using the different methods, a Mann-Whitney U-test (also known as Wilcoxon rank-sum test) (McKnight & Najab, 2010) was used. This test is non-parametric, and unlike the common t-test, does not make any assumptions related to the distribution. The null hypothesis in a Mann-Whitney U-test is that the two samples come from identical populations. A p-value (probability associated with the smallest level of significance that would lead one to reject the null hypothesis) greater than 0.05 indicates an acceptance of the null hypothesis at the significance level of 5% (or confidence interval of 95%). The p-values for the Mann-Whitney tests that compared the populations on which the porosity and pore sizes were measured were always greater than 0.05 for all the cases evaluated in this paper.

The relationship between the volumetric porosity and tortuosity of the pore system determined using the watershed algorithm on reconstructed 3D structures is shown in Figure 5-3(a). An increase in porosity is observed to decrease the tortuosity as shown in Figure 5-3(b)[1]. For the same aggregate size, an increase in porosity results in larger number of pores, thereby reducing the effective distance between the pores and thus the tortuosity. Theoretically, for a porosity of 1.0, the tortuosity also equals 1.0.

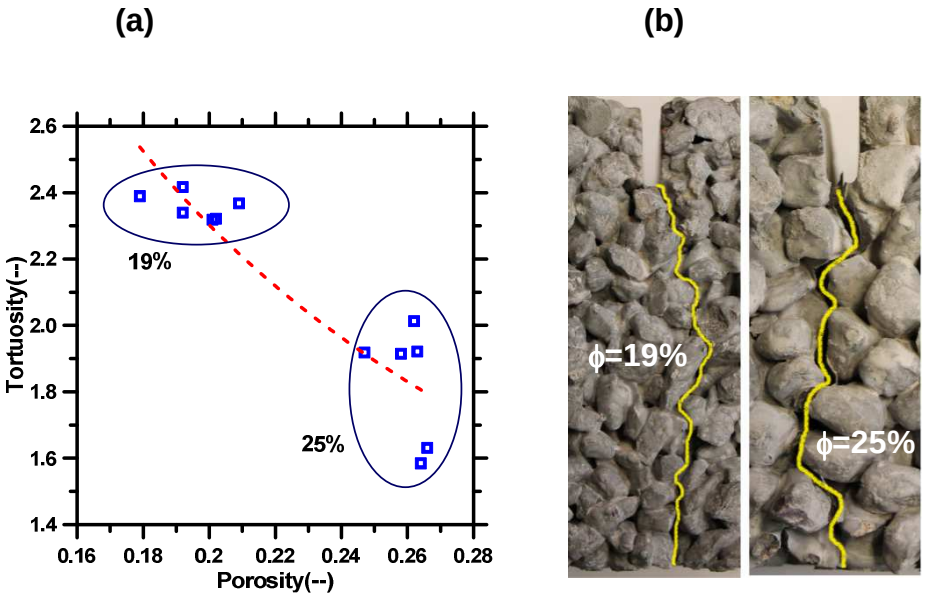

Figure 5-3: (a) Relationship between volumetric porosity and tortuosity determined using a watershed algorithm on reconstructed 3D structures; (b) crack path tortuosity for specimens with 19% and 25% porosity showing a lower (qualitative) tortuosity with increasing porosity.

[1] In Figure 5-3(b), only a 2D representation of the crack tortuosity is shown. The actual crack traverses three dimensions, depending on the pore and solid phase orientation. To show the effects simplistically, this has been intentionally avoided in the figure. However, the actual tortuosity calculations do account for this.

5.3 Compressive Strength

The compressive strengths of the 12 different pervious concrete mixtures studied here are presented in Figure 5-4(a). For a design porosity of 19%, compressive strengths in the range of 18-23 MPa is obtained, whereas for a 25% design porosity, the strength range is 10-15 MPa, which is in line with other reported studies (Omkar Deo & Neithalath, 2010). The influence of fiber volume fraction is shown in Figure 5-4(a), and as expected, the incorporation of fibers does not provide any tangible benefits to compressive strength. While the mixtures with 0.5% fiber volume do show some improvement in compressive strength at 19% porosity, it could be attributed to the slightly lower actual porosity of the mixture (See Figure 5-1). For the mixtures with a 25% design porosity, the compressive strengths slightly decrease with increasing fiber volume fraction. In highly porous mixtures, higher volume fraction of fibers likely result in fiber agglomeration, thereby spacing the solid phase further apart. The relationship between the volumetric porosity and compressive strength for all the mixtures evaluated here is shown in Figure 5-4(b), showing the well-established dependence of strength on porosity.

(a) **(b)**

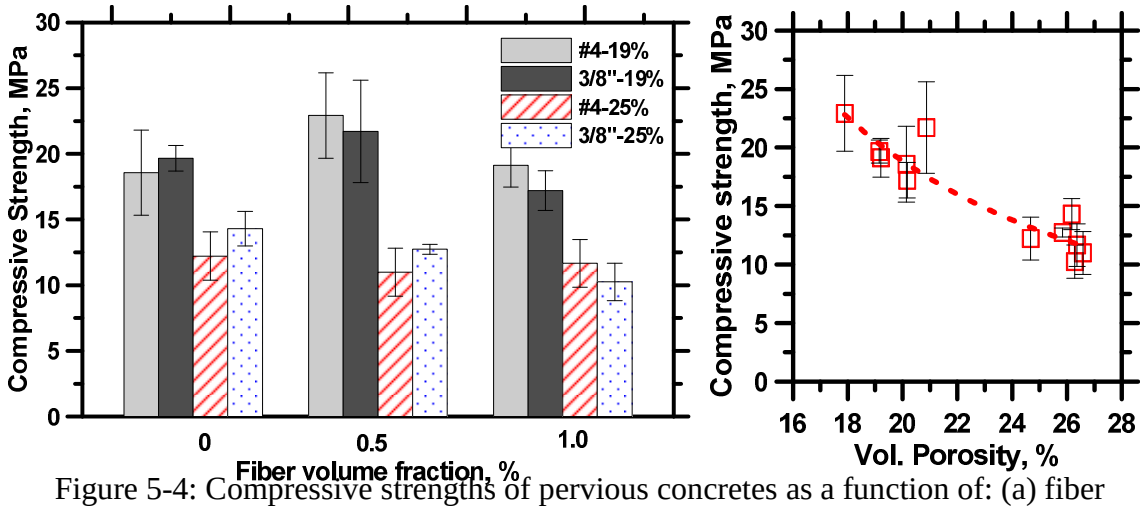

Figure 5-4: Compressive strengths of pervious concretes as a function of: (a) fiber volume fraction, and (b) porosity

5.4 Fracture Parameters: Influence of Pore Structure and Fibers

The influence of aggregate content (Elices & Rocco, 2008)(Amparano, Xi, & Roh, 2000) and porosity (Zhang & Ansari, 2006)(Usami, Kimoto, Takahashi, & Shida, 1986) on the fracture properties of porous materials including conventional concretes has been reported. The use of fibers to improve the fracture response of concretes is also well studied (Bragov et al., 2013)(Balendran, Zhou, Nadeem, & Leung, 2002)(Reis, 2006). In this research, the fracture parameters of the pervious concrete specimens, and the influence of pore structure features and flexible fiber reinforcement were studied using an effective elastic crack approach. The two-parameter fracture model used here incorporates the pre-peak non-linear behavior in a notched beam (notch size a_0) through an equivalent elastic material containing a crack of effective length a_e such that $a_e > a_0$. Based on this method, K_{IC} and $CTOD_c$ can be used to characterize the fracture behavior of pervious concretes. This section primarily makes use of the fracture parameters (K_{IC},

$CTOD_c$, and critical crack length, a_c) to bring out the influence of pore structure and fiber volume fraction on the fracture response.

5.4.1 Load-CMOD response

Figure 5-5(a)-(d) depict the representative load-CMOD responses for the notched three-point bend beam specimens of pervious concretes made using different aggregate sizes and proportioned for different porosities. The responses as a function of fiber volume for each of the mixture combinations are also shown. These figures show that the peak loads sustained by the pervious concrete notched beams are generally invariant of the fiber volume fractions in the range evaluated here. The slope of the pre-peak region in the load-CMOD response is also not very different irrespective of the fiber loading. The dependence of porosity on the peak loads is roughly similar, with an approximately 20% reduction when the porosity is increased from 19% to 25%, notwithstanding the differences in aggregate sizes (comparing Figure 5-5a and b, and Figure 5-5c and d).

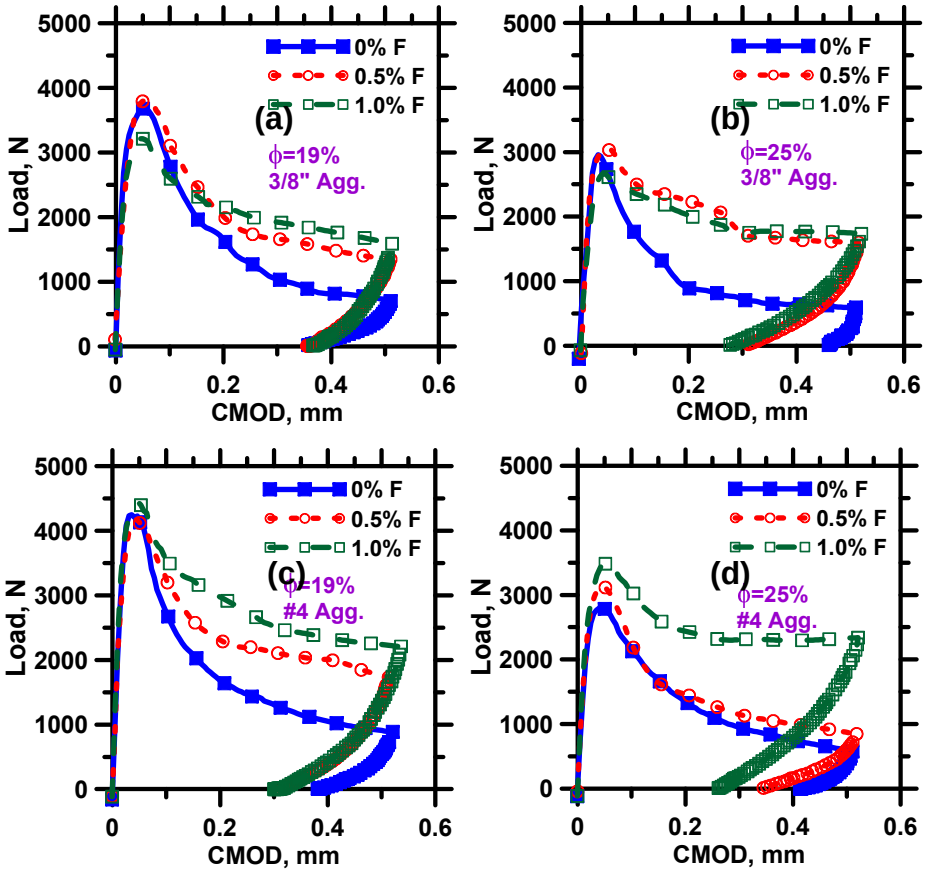

Figure 5-5: Load-CMOD relationships from which fracture parameters were derived. (a) and (b): 3/8" aggregate mixtures with 19% and 25% porosity, and (c) and (d): #4 aggregate mixtures with 19% and 25% porosity

5.4.2 Combined influence of fiber volume, porosity, and pore sizes on K_{IC} and $CTOD_c$

It is instructive to examine the combined influence of the pore structure features and fiber volume on the load-CMOD response of pervious concretes. One of the main objectives of using different volumes of synthetic fibers in these macroporous materials is to evaluate if the detrimental effects of high porosity on the mechanical properties can be alleviated to some extent. It has been shown that the effect of fibers is indistinguishable in the compressive strength results. In order to evaluate the combined influence of

porosity (ϕ) and fiber volume (v_f), the ratio of the load at a CMOD of 0.5 mm to the peak load ($P_{0.5mm}/P_{max}$) is used as one of the mechanical properties of interest. This ratio is important since it provides a measure of the residual flexural capacity of the notched beam. The porosity for the conventional concrete is taken as zero for all fiber loading levels[2]. Figure 5-6(a) and (b) demonstrate the trends of $P_{0.5mm}/P_{max}$ as a function of both ϕ and v_f for the specimens made using #4 and 3/8" aggregates respectively (i.e., for specimens consisting of smaller and larger pores respectively)

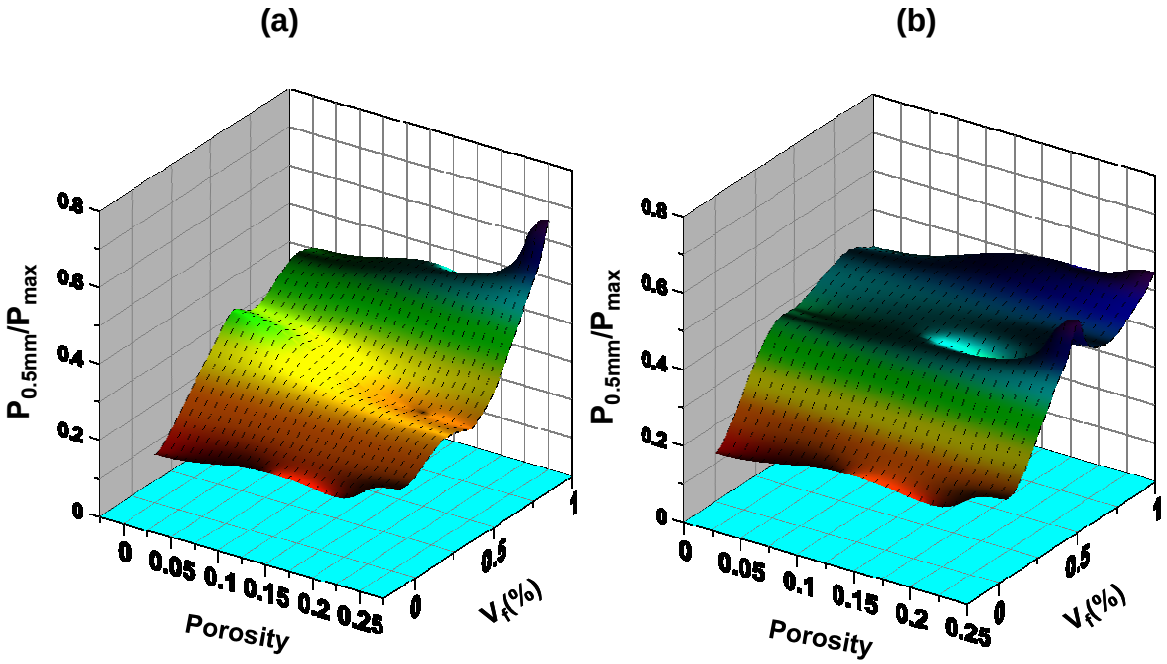

Figure 5-6: Residual flexural capacity as a function of porosity and fiber volume fraction for pervious concretes with: (a) #4 aggregates (smaller pore size), and (b) 3/8" aggregates (larger pore size).

The residual capacity is shown to be invariant with changes in porosity at a given fiber volume fraction. For example, in the absence of fibers, the residual capacity is the

[2] The porosity of conventional concretes, when compared to the large, open porosity of pervious concretes, can be safely considered to be negligible.

lowest, and the ratio does not change appreciably with changes in porosity in the range studied. The effect of fibers at a given porosity is very evident from these figures. For conventional concretes (corresponding to zero porosity in these figures), the residual capacity ratio increases from 12% to 40% when the fiber volume is increased from 0 to 1.0%. For the pervious concretes with 19% and 25% porosity, the increase in residual capacity ratio varies from 15-50% and 20-65% respectively when the fiber volume is increased from 0 to 1.0%. Thus it can be noticed that the contribution of fibers towards enhancing the residual capacity increases with an increase in the specimen porosity, providing an insight into the synergistic effects of fibers and pore volume fraction on the fracture performance of pervious concretes. The explanation of this behavior is based on the fact that, increasing the porosity while maintaining the aggregate size (or the pore size) same implies more number of pores, thereby reducing the mean free spacing between the pores. The statistical possibility that the fibers aid in bridging these pores and transfer load across the pores is higher when the pores are closer to each other. Thus the fibers are more effective at higher porosities with respect to the flexural load capacity.

The fracture toughness (K_{IC}) of the pervious concrete mixtures as a function of the fiber volume fraction is shown in Figure 5-7. Figure 5-7(a) and (b) show that, for both the porosities and both the aggregate sizes (or pore sizes), K_{IC} increases with fiber volume fraction. It is also noticed that, for the same porosities, an increase in pore size (3/8” aggregate specimens have a larger critical pore size than the #4 aggregate specimens, as shown in Figure 5-2) results in a reduction in K_{IC} values. This can be explained based on the idea of pore-to-pore tortuosity shown Figure 5-3. Considering that

the aggregates in pervious concretes are fracture resistant (the dominant crack path in the solid phase is through the paste binding the aggregates), and since the paste thickness in pervious concretes is very small (Yang & Jiang, 2003), the pore-to-pore tortuosity can be used as a representation of the crack path tortuosity. This is because the advancing crack either traverses the pore, or if the pore size and orientation with respect to the crack is favorable (generally for much smaller sizes than those encountered in pervious concretes made using the aggregate sizes as described in this paper), crack blunting occurs which drives the crack along the pore-solid interface. When the solid ligament lengths are small, as is the case in pervious concretes and especially with specimens having larger pore sizes, the crack traverses from one pore into another, leading to an instantaneous initiation from this pore. This continuing mechanism drives the crack through the specimen. Thus the pore-to-pore tortuosity can be considered to be an appropriate measure of the crack path distance. For the same porosity, a larger pore size results in lower tortuosity values, and correspondingly, lesser distance for the crack to travel. The material structure does not facilitate increased dissipation of the energy of the crack, thereby leading to lower K_{IC} values. The tortuosity, and thus the crack path traversed are longer in a specimen with smaller pore sizes, creating the opposite effect. Figure 5-3(b) shows the crack tortuosity in pervious concretes of same porosity, made using the different aggregate sizes to qualitatively reinforce this point.

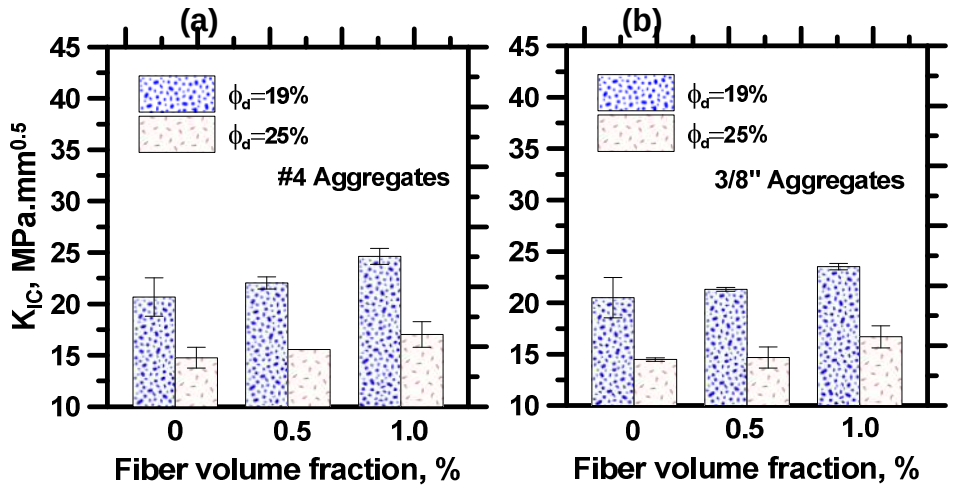

Figure 5-7: K_{IC} as a function of fiber volume for pervious concrete mixtures made using: (a) #4 aggregates, and (b) 3/8" aggregates.

A bubble plot showing the dependence of K_{IC} on the porosity, pore sizes, and fiber volume is shown in Figure 5-8(a). The larger the size of the bubble in this plot, the larger is the K_{IC} value. Expectedly, this plot shows that the K_{IC} values are higher when the porosity is lower and the fiber volume fraction is higher. It can be noticed that, even though there is a synergistic effect of fibers at a higher porosity as shown in Figure 5-5, the overall benefits of having a lower porosity far outweigh this effect. At a higher fiber volume and a lower porosity, the pore sizes do not come into play to large extent because the tortuosity of the pore network is larger and energy is spent by the crack in traversing longer distances. In a forthcoming section, all of this information is used as inputs into a statistical model and a stochastic simulation to quantify the relative sensitivity of the pore structure features and fibers on the fracture toughness of pervious concretes. The influence of the pore structure features and fibers on the $CTOD_c$ values is quite different

from those on the K_{IC} values as can be noticed from Figure 5-8(b). The effect of porosity is much less pronounced on the $CTOD_c$ values.

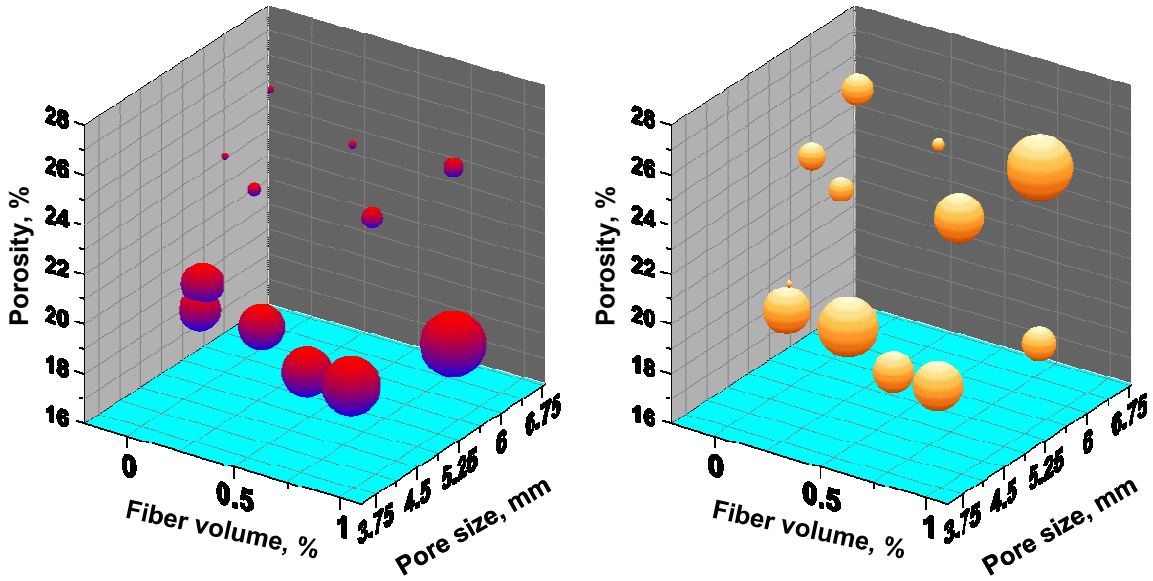

Figure 5-8: Bubble plots showing the combined influence of porosity, pore sizes, and fiber volume on: (a) K_{IC}, and (b) $CTOD_c$ of pervious concrete mixtures. The larger the bubble size, the larger the K_{IC} or $CTOD_c$ value. The bubble size range is maintained the same in both the figures for consistency.

Since K_{IC} and $CTOD_c$ are the critical fracture properties of a quasi-brittle material like concrete, it is useful to explore their relationship. Ideally, K_{IC} and $CTOD_c$ depend only on the material. As can be observed in Figure 12, among the material properties, K_{IC} is primarily dependent on the porosity (also shown in Figure 5-8), with the values almost unchanged even when the $CTOD_c$ values change with increase in aggregate size and fiber volume. The higher $CTOD_c$ values are typically observed for the specimens with higher fiber volume fraction. It is worthwhile to mention here that $CTOD_c$ is defined as the

crack opening displacement at the critical fracture load. The fibers will delay the opening, propagation, and coalescence of some of these cracks, thereby accommodating a larger crack opening displacement before failure.

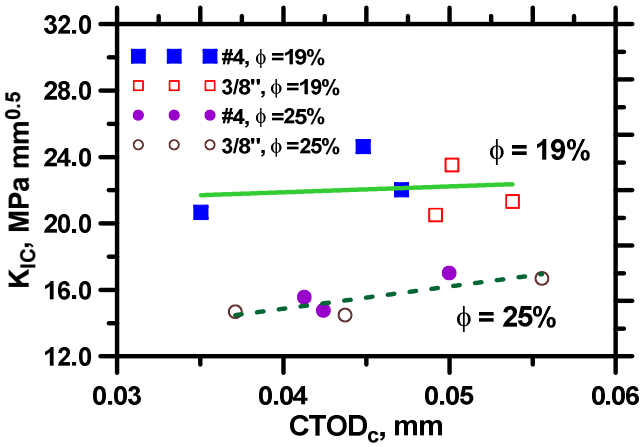

Figure 5-9: Relationship between K_{IC} and $CTOD_c$ for the pervious concrete mixtures

5.5 Crack Extension and R-Curve Behavior of Pervious Concretes

Figure 5-10 depicts the critical effective elastic crack length, a_c (crack length at the peak load) as a function of the fiber volume fraction. The critical crack length increases with an increase in fiber volume. For an ideally brittle material, the critical crack extension is zero. Thus it is only natural that the critical crack length (or the extension) increases with fiber volume because fibers increase the ductility of the material.

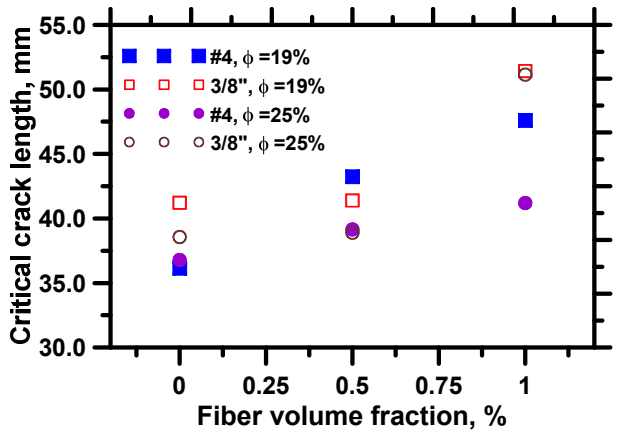

Figure 5-10: Relationship between critical crack length and fiber volume fraction for the pervious concrete mixtures

In order to further quantify the influence of porosity and fibers, the stress capacity of the specimens as a function of crack length was determined. This provides an indication of the crack length "tolerability" of the material. The effective crack length (a_e) corresponding to every CMOD value in the load-CMOD curve was determined based on the focal point method shown in Figure 5-1(b). An "imaginary" unloading compliance for every point in the load-CMOD curve (C_{ux}) was calculated by joining the focal point to the corresponding point in the curve and determining the inverse of its slope. The same procedure that was used to obtain a_c in Section 2.3 was used here to obtain a_e; the only difference being the use of a different value of C_u corresponding to every CMOD value. The stress capacity of the specimen as a function of crack extension ($\Delta a = a_e - a_0$) is shown in Figure 14(a). Only the results for pervious concrete specimens made using #4 aggregates are shown here to keep the discussion succinct. Very distinct trends are observed for the lower and higher porosity specimens (the solid lines in Figure 5-11(a)), with the lower porosity specimens showing a higher stress capacity for the same crack

extension. The influence of fibers, as expected, is minimal in the pre-peak region. For the same effective crack length, the fiber reinforced pervious concrete specimens have a higher stress capacity, or in other words, the incorporation of fibers result in the pervious concrete specimens being able to tolerate a larger crack extension at the same stress. The influence of fibers becomes more prominent when the crack extension increases, irrespective of the specimen porosity. While the tails of the stress-Δa curve for the non-fiber reinforced specimens are essentially parallel, they are likely to meet at some large crack extension (i.e., have the same stress) for the fiber reinforced pervious concretes. This shows that, when the crack extension approaches a large value, the porosity (in the considered range) is less consequential for fiber reinforced pervious concretes. The increased influence of fibers in the larger porosity specimens is evident here, which is in line with the results reported in a previous section on the residual load capacity.

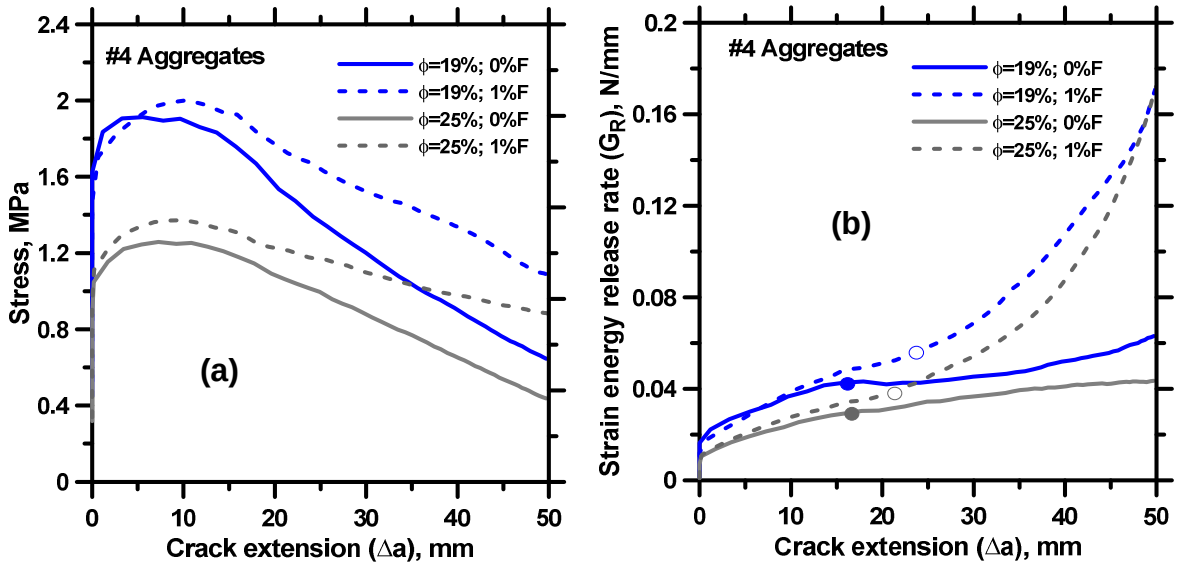

Figure 5-11: (a) Stress, and (b) Strain energy release rate, as functions of crack extension for the pervious concretes made using #4 aggregates. The symbols in (b) correspond to the crack extension at the peak load.

R-curves that indicate the change in fracture resistance in terms of the strain energy release rate G_R as a function of crack extension are shown in Figure 5-11(b) for the pervious concrete specimens made using #4 aggregates, with and without the incorporation of fibers. The behavior of specimens made using 3/8" aggregates are very similar (albeit with differences in magnitude) and hence are not discussed here. R curves have been used to characterize toughening in fiber reinforced concrete and other composites (Eissa & Batson, 1996)(Llorca & Elices, 1990)(Mobasher & Peled, 2004). The R-curve is not a material parameter and is geometry-dependent, but can be used to compare the fracture resistance of pervious concretes in this case because the testing geometries were identical for all the specimens. The critical crack extension (Δa at the peak load) is represented in these curves using symbols. The strain energy release rate was calculated as:

$$G_R = \frac{\sigma^2 \pi a}{E}[F(a_0 / d)]^2 \qquad 5.1$$

The function $F(a_0/d)$ is the geometric function for the stress intensity factor (Shah et al., 1995). The R curves shown in Figure 5-11(b) demonstrate three distinct regions. In the first region, there is a small increase in fracture resistance without any crack extension, attributable to the bridging forces behind the crack tip. In the second region, there is a gradual increase in fracture resistance with increase in crack extension. This region ends roughly at the crack extension corresponding to the peak load (marked using symbols),

after which the behavior of fiber-reinforced and non fiber-reinforced specimens diverge significantly. As can be seen from Figure 5-11(b), the G-Δa relationship depends only on the porosity and is independent of the fiber volume until the end of the second region (peak load). The third region for the specimens without fiber reinforcement is a plateau, with little to no further increase in fracture resistance with increasing crack length. This stage corresponds to rapid propagation of the crack. However, for fiber reinforced pervious concretes, there is a much larger increase in fracture resistance with crack extension in the third region. This is attributed to the influence of fibers on the post-peak response of concretes that result in toughening. It can be noticed from the R-curves shown here that for fiber reinforced pervious concretes, the larger porosity specimen has a fracture resistance that approaches that of the lower porosity specimen at higher crack extensions, once again demonstrating the larger influence of fibers in mixtures having a higher porosity.

5.6 Quantification of the Influence of Material Design Variables on K_{IC}

The preceding sections have analyzed the influence of pore structure features of pervious concretes and the fiber volume fraction on the fracture parameters extracted from the two-parameter fracture model. In this section, effort is made to stochastically quantify the sensitivity of each of the material design variables to the fracture parameters, especially K_{IC}. Understanding the relative influence of each of the material design parameters on the fracture toughness will help optimize the pore structure of pervious concrete for mechanical performance.

5.6.1 A deterministic model relating K_{IC} and material design variables

The development of a deterministic starting model that relates K_{IC} to the parameters of interest in necessary before the feature sensitivity can be stochastically evaluated. A regression-based method is chosen to accomplish this objective. All the pore structure features described earlier (porosity, pore size, mean free spacing of pores, tortuosity) along with the fiber volume fraction have been used in the model. Several statistical models were evaluated, and a multiple non-linear regression model was found to provide the highest degree of predictive capability. However, the use of all the terms individually in a multiple regression model resulted in multi-collinearity issues. Multi-collinearity is a phenomenon in which two or more model terms are highly correlated to each other, and this correlation coefficient is greater than the correlation of these terms with the response variable (Omkar Deo & Neithalath, 2010)(Kumar, 1987). Though multi-collinearity does not reduce the predictive capability of the model, it has the potential to interfere with the assignment of sensitivity to the individual variables. Table 5-1 shows the correlation matrix of the non-linear regression model containing all the individual model terms. The parameter interactions were ignored since they were observed not to contribute much to the statistical significance of the model. The terms in bold in Table 1 show the model terms demonstrating multi-collinearity.

In order to avoid multi-collinearity, the following actions were performed: (i) pore structure features were grouped based on their physical relationships so as to result in reduced inter-variable correlation coefficients, and (ii) transformations applied to the model terms and/or the response variables to ensure the significance of the model and to

reduce the effects of multi-collinearity. Since the pore size (d_{crit}) and the mean free spacing of pores (λ) are both indicators of characteristic length scale of the phases in pervious concretes (d_{crit} is a representative length scale for the pores, and λ is a representative length scale for the solid phase), the ratio (λ/d_{crit}) is included as a non-dimensional term in the model. Similarly, since it was shown that the porosity and tortuosity are well related, ϕ/τ was included as another term. The correlation matrix for the transformed model is also shown in Table 1, with the multi-collinearity issues being mostly resolved. The correlation between λ/d_{crit} and v_f is slightly higher than that between λ/ d_{crit} and K_{IC}, but it has been ignored here considering the adequacy of the model and the high R^2 value (0.96) of prediction as shown in Figure 5-12: Experimental and predicted values of KIC for all the pervious concrete specimens using the statistical model. The response variable is also transformed by a power term β, which is equal to -½. The transformed model is expressed as:

$$(K_{IC})^{\beta} = \alpha_0 + \alpha_1 v_f + \alpha_2 \frac{\phi}{\tau} + \alpha_3 \frac{\lambda}{d_{crit}} \qquad 5.2$$

An analysis of variance found the model terms to be all significant with p-values far lesser than 0.05. The coefficients α_0, α_1, α_2, and α_3 were obtained as 4.42, 34.76, -11.31, and 2.30 respectively.

Table 5-1: Correlation matrix for the non-transformed and transformed models for K_{IC} as a function of the experimental variables. The values in bold indicate multi-collinearity.

Model	Model Terms	ϕ	d_{crit}	λ	τ	v_f	K_{IC}
Non-Transformed model (with	ϕ	1.00					
	d_{crit}	**0.26**	1.00				

separate features)	λ	0.59	**0.62**	1.00			
	τ	**0.92**	**0.56**	**0.70**	1.00		
	v_f	0.06	**0.23**	0.09	0.12	1.00	
	K_{IC}	0.90	0.15	0.63	0.82	0.33	1.00
Transformed model (pore structure features grouped and transformations applied)	Model Terms	ϕ/τ	λ/ d_{crit}	v_f	K_{IC}		
	ϕ/τ	1.00					
	λ/ d_{crit}	0.06	1.00				
	v_f	0.13	**0.35**	1.00			
	K_{IC}	0.84	0.33	0.33	1.00		

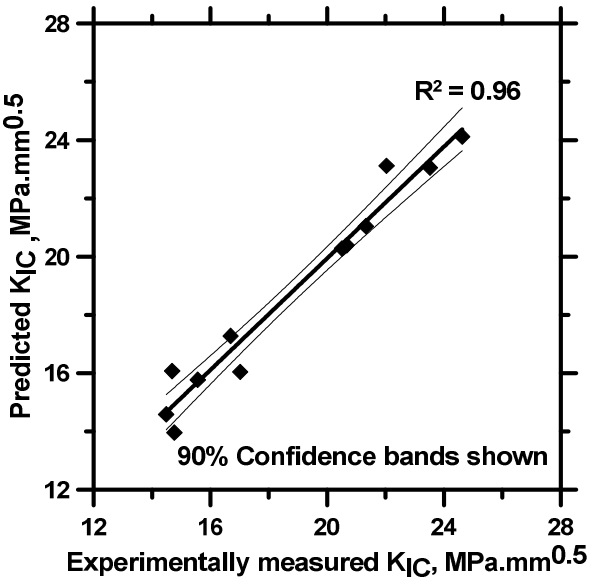

Figure 5-12: Experimental and predicted values of K_{IC} for all the pervious concrete specimens using the statistical model

5.6.2 Analyzing feature sensitivity through stochastic simulation

In this section, the use of a Monte-Carlo simulation to understand the sensitivity of the model terms on the predicted K_{IC} values is discussed. The deterministic model

described in the previous section is used as the base model. For each of the model parameters, the Anderson-Darling (A-D) statistic is calculated for several probabilistic distribution fits (including normal, lognormal, Weibull etc.), and the distribution showing the lowest A-D statistic shows the closest fit to the data (Hosmer Jr, Lemeshow, & May, 2011). For all the three terms (v_f, ϕ/τ, λ/d_{crit}) in the transformed model for K_{IC}, normal distribution was found to be the best one representing the data. Each of these three terms was randomly generated 10,000 times based on the parameters of their probability distributions, to determine the probability distribution of K_{IC}. Figure 5-13(a) shows the predicted histogram of probability distribution for 10,000 trials. The predicted K_{IC} values also follow a normal distribution. The contribution of variance or the sensitivity of the model parameters to the K_{IC} values is shown in Figure 5-13(b). The sensitivities were determined by using the statistical forecasting tool, Crystal Ball™. The percentage sensitivity plotted in this chart, calculated by computing the rank correlation coefficients between every input model term with the estimate of K_{IC}, provides a meaningful indication of the magnitude and direction of changes in K_{IC} with changes in each of the input terms. Positive sensitivities indicate that an increase in the input model term is associated with an increase in the output term. The larger the absolute value of the percentage (%) sensitivity, the stronger is their correlation or interdependency. Even when the number of trials in the Monte-Carlo simulation was increased to 20,000, the sensitivities were found to be unchanged. The term that influences K_{IC} the most is ϕ/τ, and an increase in this parameter decreases the K_{IC} value as shown by the negative sensitivity. Since the tortuosity decreases with increase in porosity, the term ϕ/τ is

amplified even with a slight increase in porosity or decrease in tortuosity, explaining the larger magnitude of sensitivity associated with this term. Increase in the mean free spacing between the pores or the solid phase spacing or decrease in pore size are found to increase K_{IC}, as is the increase in volume fraction of fibers. The quantification of feature sensitivities provided here reinforces the conclusions made in the earlier sections on the influence of the pore structure features and fiber volume on K_{IC} of pervious concretes.

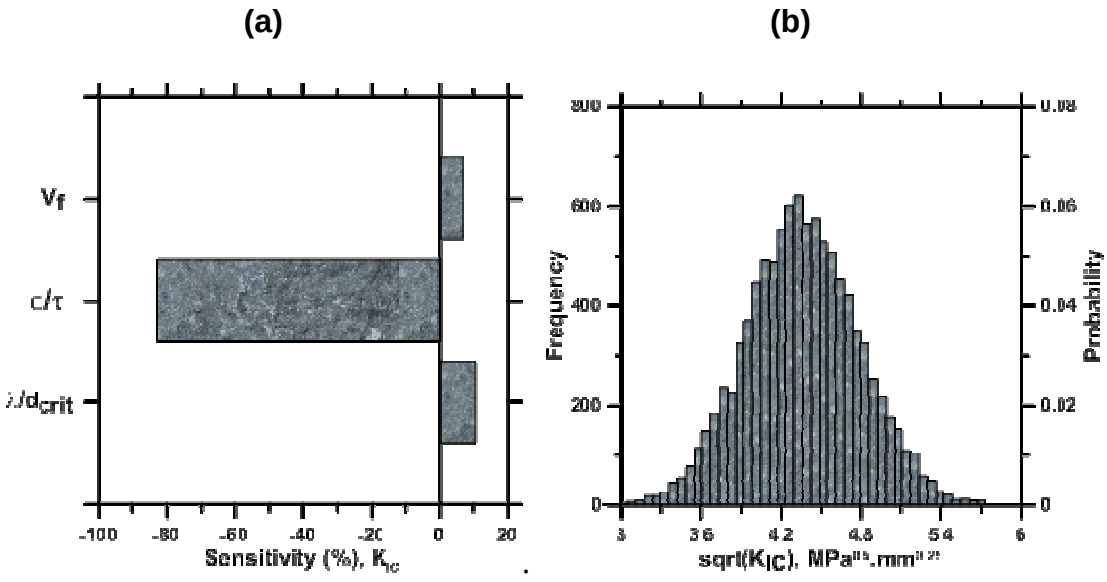

Figure 5-13: (a) Predicted histogram for K_{IC} using Monte-Carlo simulation, and (b) sensitivity of the model parameters to K_{IC}

5.7 Summary

The fracture response of pervious concrete specimens proportioned for different porosities, as a function of the pore structure features and fiber volume fraction, was studied in this chapter. Stereological and morphological methods were used to extract the relevant pore structure features of pervious concretes from planar images. A two-

parameter fracture model was used to obtain the fracture toughness (K_{IC}) and critical crack tip opening displacement ($CTOD_c$) from load-crack mouth opening displacement (CMOD) data of notched beams under three-point bending. The experimental results show that K_{IC} is primarily dependent on the porosity of pervious concretes. For a similar porosity, an increase in pore size results in a reduction in K_{IC}. At similar pore sizes, the effect of fibers on the post-peak response is more prominent in mixtures with a higher porosity, as shown by the residual load capacity, stress-crack extension relationships, and G_R curves. These effects were explained using the mean free spacing of pores and pore-to-pore tortuosity in these systems. A sensitivity analysis was employed to quantify the influence of material design parameters on K_{IC}.

6 CHAPTER 6: FRACTURE ENERGY

6.1 General

Multi phase materials such as concrete and rock are quasi-brittle and there is a non-linear aspect to the propagation of the crack where there is plastic zone of semi-ductile behavior. In the following chapter, a fracture energy release rate (G_f) based on non linear fracture mechanics models for quasi-brittle materials, and is classified as a fictitious crack approach, was determined for various types of pervious concrete and with varying amount of fibers (Shah et al., 1995)(Wittmann, 2002)(Hillerborg et al., 1976).

6.2 Pore Structure Features

The effect of aggregate size, porosity and addition of fibers on the influence of critical pore diameter was analyzed in great depth. The critical pore diameter was calculated from the scanned images using both the two-point correlation function and granulometric morphology which were explained in detail above. For each mix design, there were approximately 8 scanned images that were used for granulometry and TPC. It was first found that there was no significant deviation from the critical pore diameters calculated from either TPC or granulometry by using a Mann-Whitney two tailed U test (Kruskal, 1957). If the non-parameteric measure of the overlap between the two distributions (P-value) was greater than 0.05 it could be determined that the two populations were statistically similar.

The critical pore diameters were compared to the size of aggregate used and its volumetric porosity as well as the fiber content volume used to see if a relationship could

be observed. The reason for using different aggregate sizes in pervious concrete is to get different average pore sizes. Pore size is usually directly proportional to the aggregate size but has no relation to the volumetric porosity.

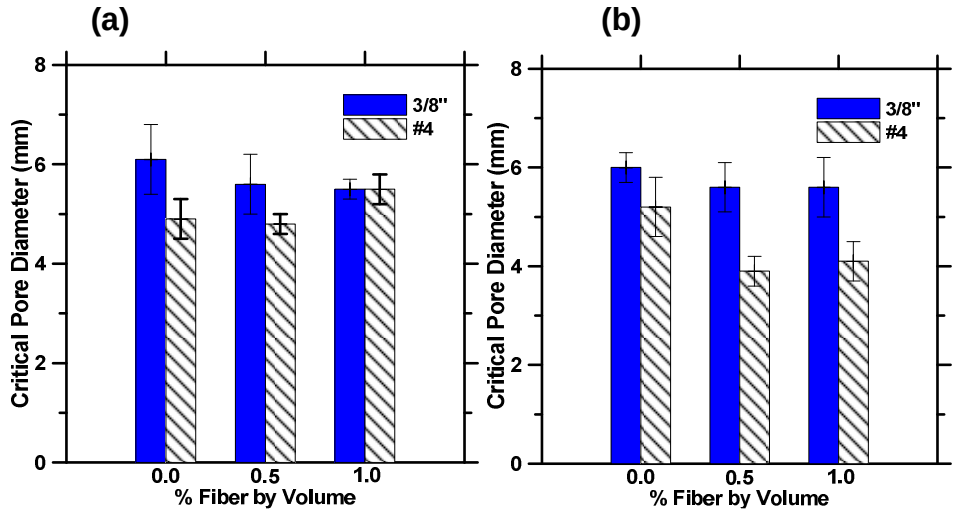

Figure 6-1: Critical pore diameter vs. % fiber by volume for a) 19% porosity and b) 25% porosity

The tortuosity has an inverse relationship to the porosity. When the porosity is one hundred percent it will be have a minimal value of 1 for the tortusoity (Epstein, 1989b). In Figure 6-2(b) the tortuosity can be seen to decrease in hyperbolic manner as the porosity increases. The tortuosity only seems to be a function of porosity and not of fiber content or aggregate though it does appear that at the higher porosity, the larger aggregate size has the higher tortuosity. At the lower porosity of 19% there is no significant difference in tortuosity with aggregate size and this can be observed in Figure 6-2(a).

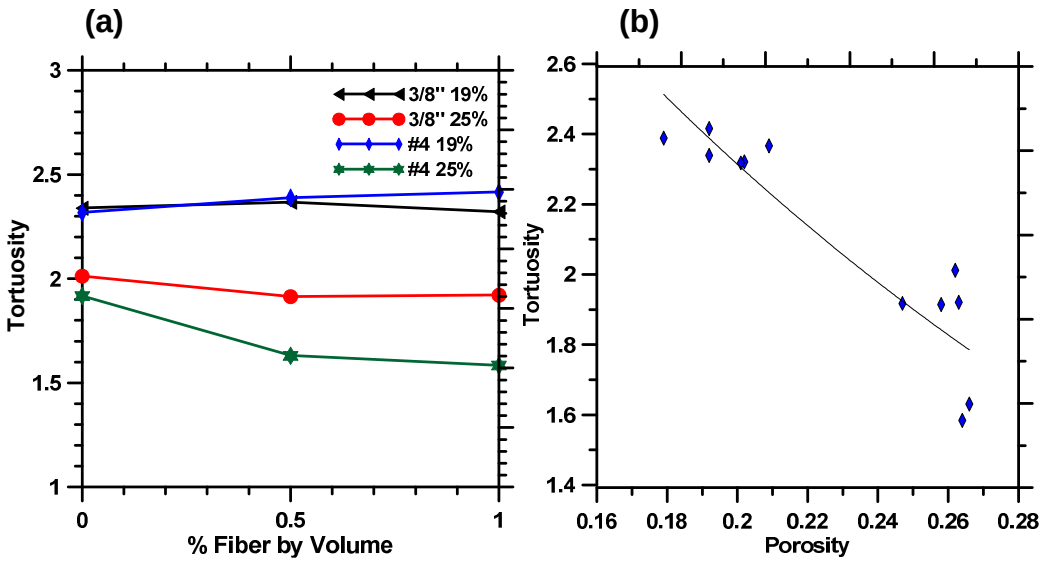

Figure 6-2:(a) tortuosity vs. Fiber volume and (b) Tortuosity vs. porosity

6.3 Influence of Porosity

The influence of porosity on the peak load is of great significance. The peak load decreases by almost 50% when the porosity increases from zero to 19%. There is only a modest decrease in strength when the porosity increases from 19% to 25%. A higher porosity reduces the gel space ratio and thus reduces overall tensile strength which is consistent with the data below in Figure 6-3. (ROY & GOUDA, 1973)(Manning & Hope, 1971). The stiffness is also highly dependent upon the porosity as well. The solid concrete specimens show the greatest stiffness from the slope of the loading portion of the curve and the 25% porosity specimens have the least stiffness.

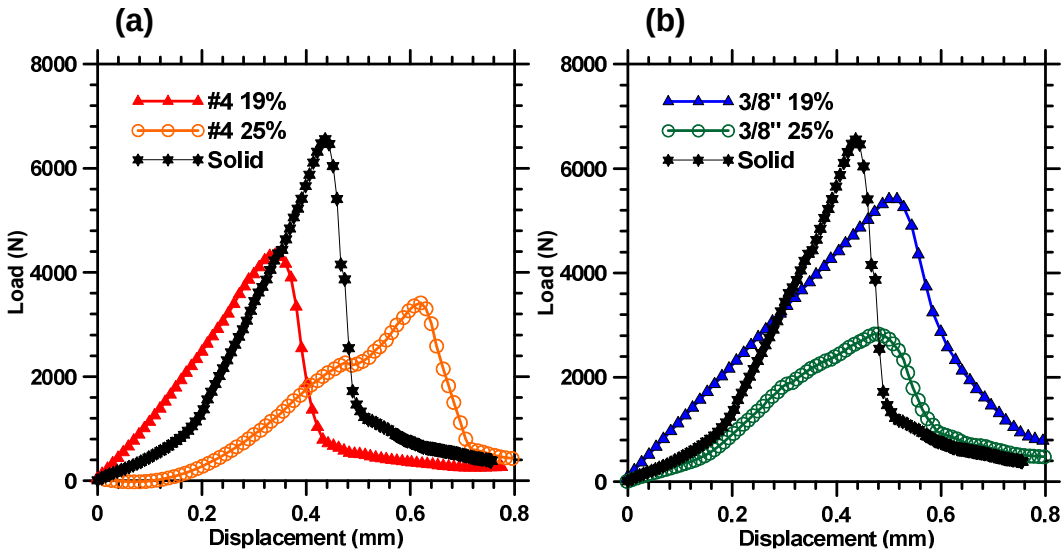

Figure 6-3: Load vs. Displacement for (a) #4 aggregate and (b) 3/8" aggregate

6.4 Influence of aggregate/pore size

The aggregate size dictates the average pore size and plays a significant role in influencing the peak load. The smaller aggregate size seems to show a moderate increase in strength with the 0.2d notch depth and 25% porosity but less strength with the 19% porosity. With the 04.d notch depth, there is a slight increase in strength with the smaller aggregate size for both the 19 and 25% porosities. It has been found in previous studies that at a given porosity, the strength of porous materials decreases linearly with the size

of the macropore(Liu, 1997). The stiffness seems to be relatively unaffected by the aggregate size for either notch depth.

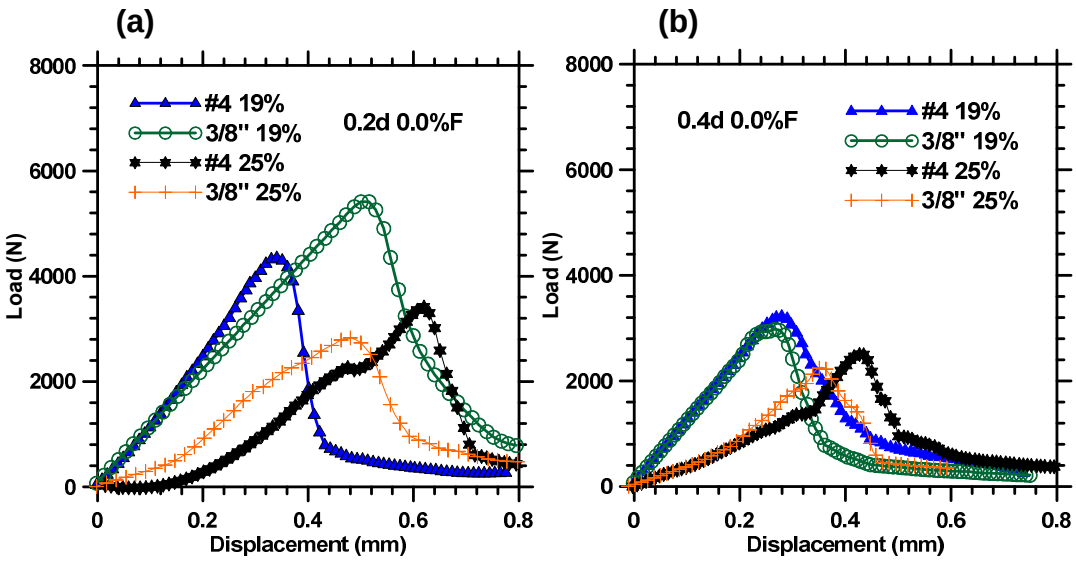

Figure 6-4: Load vs. Displacement for (a) 0.2d notch depth and (b) 0.4d notch dept

6.5 Influence of fiber volumes

The peak loads can be seen below in Figure 6-5(a) and (b). For both the 9% and 25% porosities, there is a slight decrease in peak load with increasing fiber volume. This is likely due to fiber clumping during the mixing process which weakens areas of the matrix interface. The notch depth also plays a significant role in influencing the peak

load which decreases with increasing depth. A larger notch depth will create a smaller cross section which will lower the peak load in order to keep the stress at failure the same.

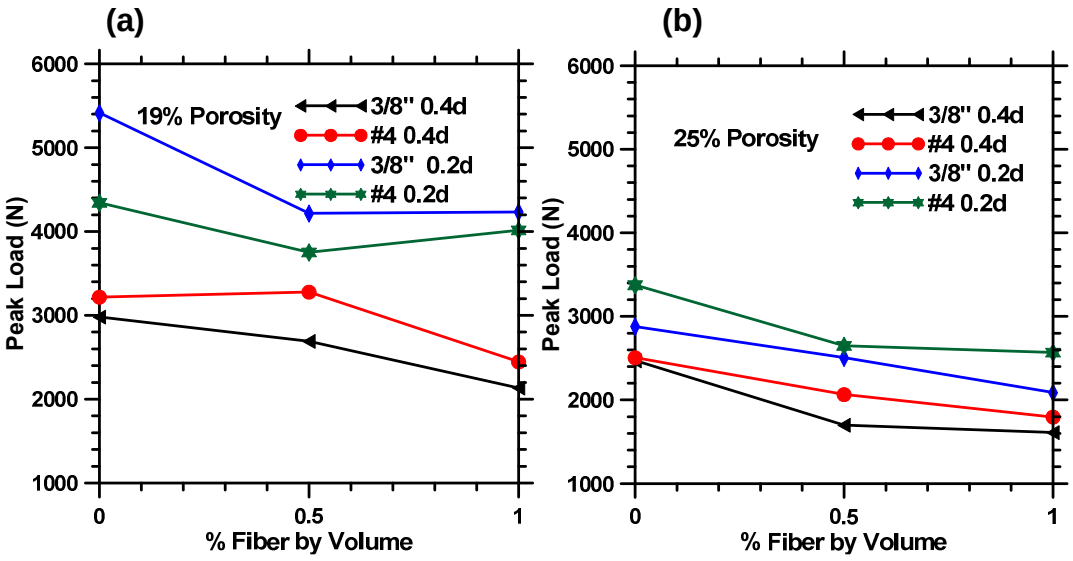

Figure 6-5: Peak load vs. % fiber volume for (a) 19% and (b) 25%

Below in Figure 6-6 the load vs. displacement curves can be seen for all 0.2d notch depth specimens. The addition of fibers increases both the stiffness and post peak strength. The number 4 sized aggregate specimens show relatively no change in peak strength but there is considerable increase in post peak strength. When the fiber content is increased to 1.0% there is significant strain hardening which is a phenonom in which

the energy needed to open a critical crack is more than the energy needed to form a new crack. The strain hardening is likely due to fiber debonding which orginates from fiber surface abrasion at fiber/matrix interface(Lin & Li, 1997)(Tjiptobroto & Hansen, 1993).

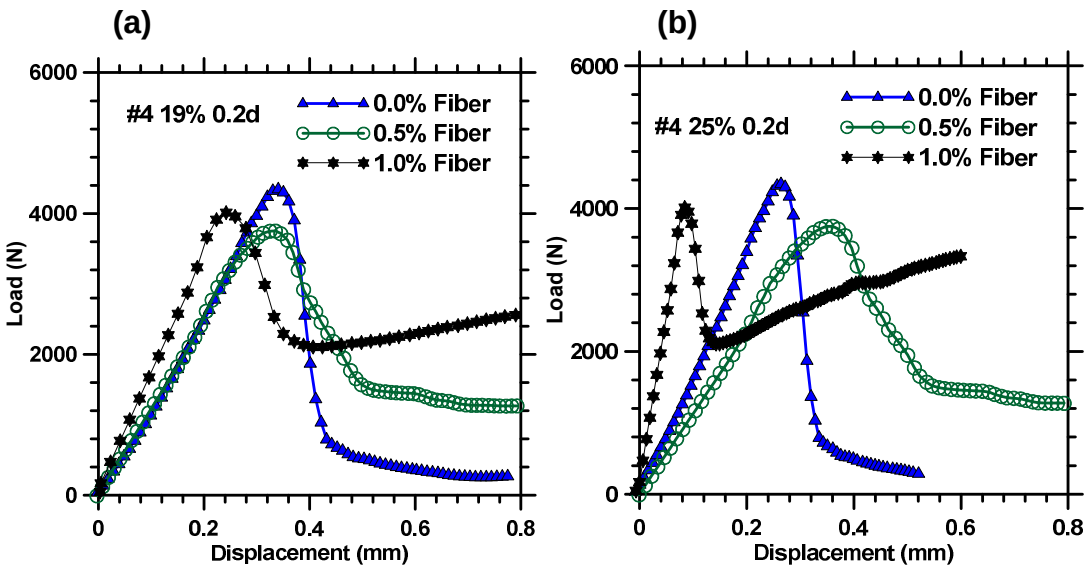

Figure 6-6: Load vs. displacement for #4 aggregate and 0.2d notch depth with (a) 19% porosity and (b) 25%

There is less strain hardening with the larger 3/8" aggregate size with 19% porosity and no strain hardening with the 25% porosity. The larger pore size allows for less fiber bridging and thus less fiber de-bonding that lead to strain hardening during the fiber pull out process.

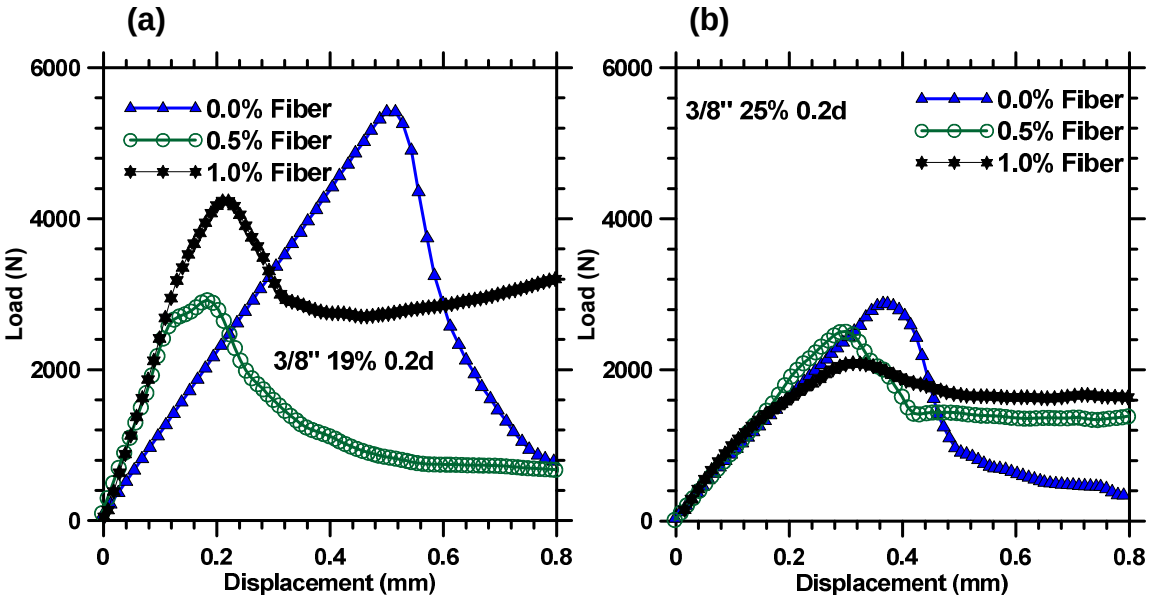

Figure 6-7: Load vs. displacement for 3/8" aggregate and 0.2d notch depth with (a) 19% porosity and (b) 25%

notch depth specimens. No strain hardening was observed with this notch depth and was likely due to less cross sectional area to give rise to a significant amount of fiber de-bonding that would result in strain hardening effects.

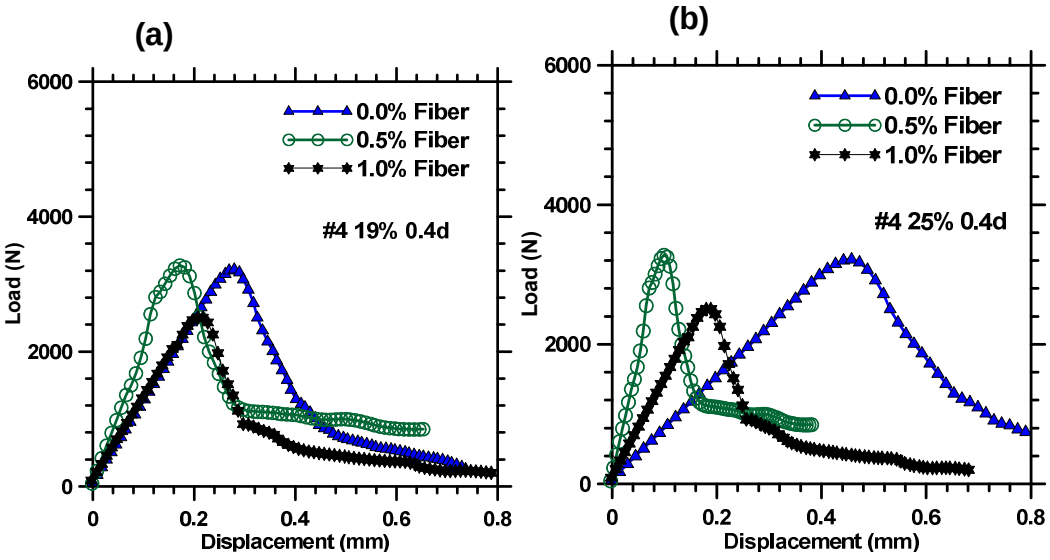

Figure 6-8: Load vs. displacement for #4 aggregate and 0.4d notch depth with (a) 19% porosity and (b) 25%

The stiffness increases with the increase in fiber volume for the higher porosity for the smaller aggregate size as can be seen above. There is very little difference in the peak strength between the 19 and 25 percent porosities. As can be seen below there is a significant decrease in peak load with the increase in porosity.

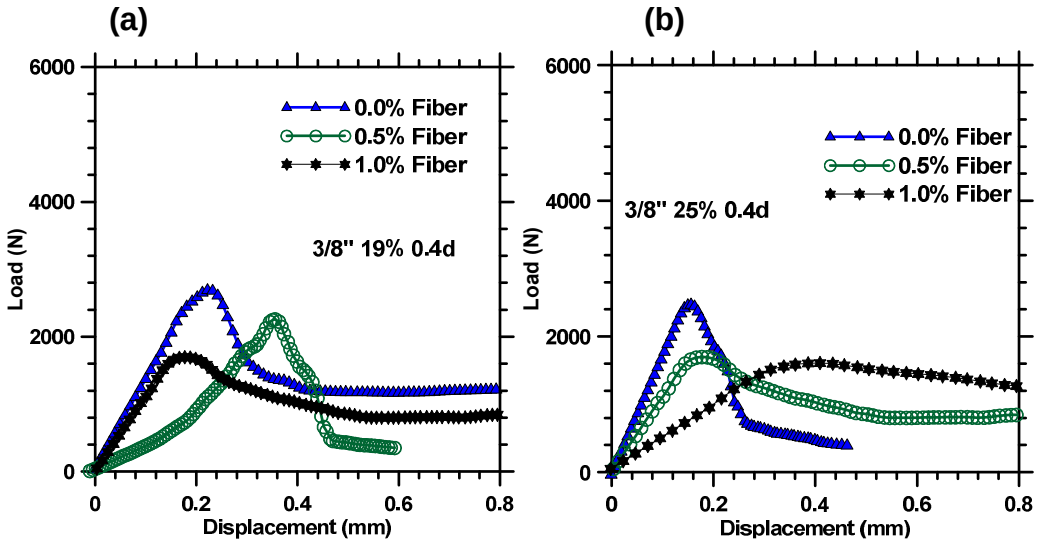

Figure 6-9: Load vs. displacement for 3/8" aggregate and 0.4d notch depth with (a) 19% porosity and (b) 25%

As can been in Figure 6-10, The toughness index I_5 is plotted against the percentage of fiber volume for the 4 different mix designs and 2 different notch depths. All specimens show significant increases in residual strength.

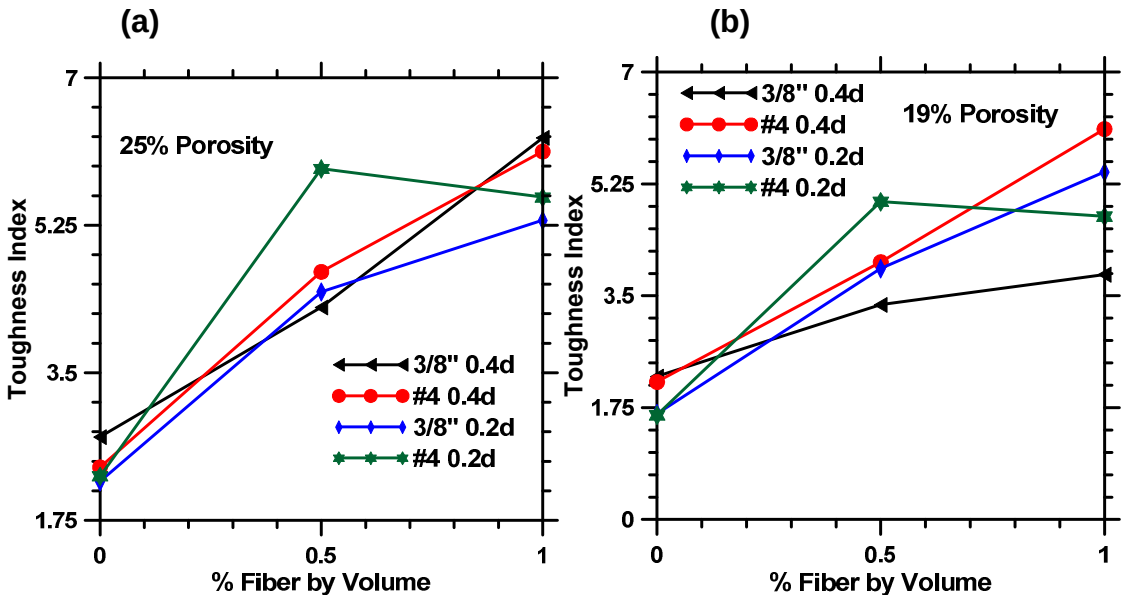

Figure 6-10: toughness index vs. fiber volume for (a) 25% and (b) 19%

As can be seen below in Figure 6-11 there is an overall increase in the fracture energy release rate with increasing fiber volume for both notch depths and aggregate sizes at 25% porosity. There is a much larger increase though at the larger notch depth and is likely due to the decreased cross-sectional area that is able to absorb and the energy released from the propagation of the of crack. There is also a slight decrease in fracture energy on the #4 sized aggregate with 0.2d notch when increasing from 0.5 to 1.0 percent fiber volume. This may be due to fiber clumping effects.

(a) **(b)**

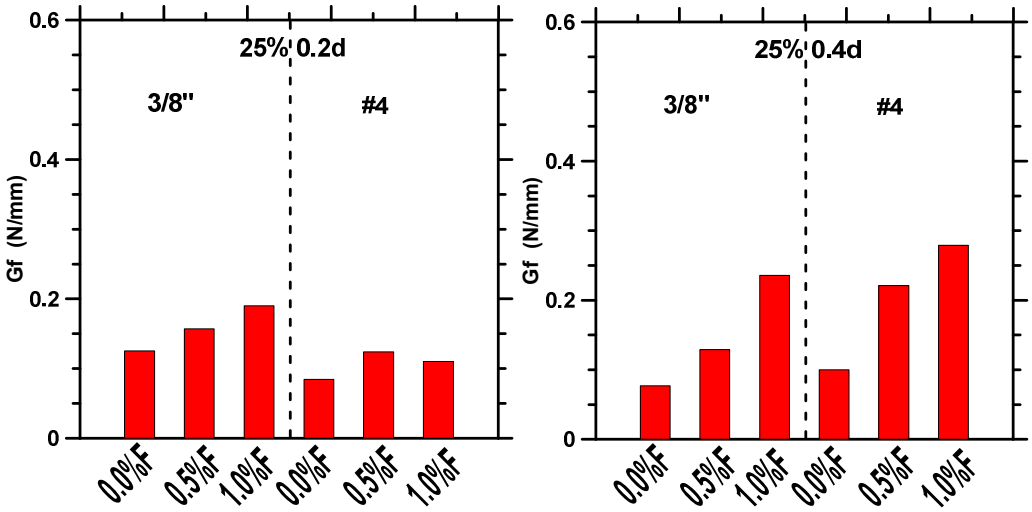

Figure 6-11: G_f at 25% porosity with a notch depth of (a) 0.2d and (b) 0.4d

Below inFigure 6-12 the G_f values for the 19% porosities can be seen. Again there is an overall increase in fracture energy when the fiber volume is increased. The larger notch depth shows less of an increase in fracture energy than with the smaller notch. It seems that with a lower porosity and fewer pores, there are fewer places to allow fiber bridging to occur so a larger cross sectional area is needed to increase the rate of energy release from the crack propagation. The fracture energy is plotted as function of fiber volume in Figure 6-13 and show the general increasing trend of G_f with the addition of fibers.

(a) **(b)**

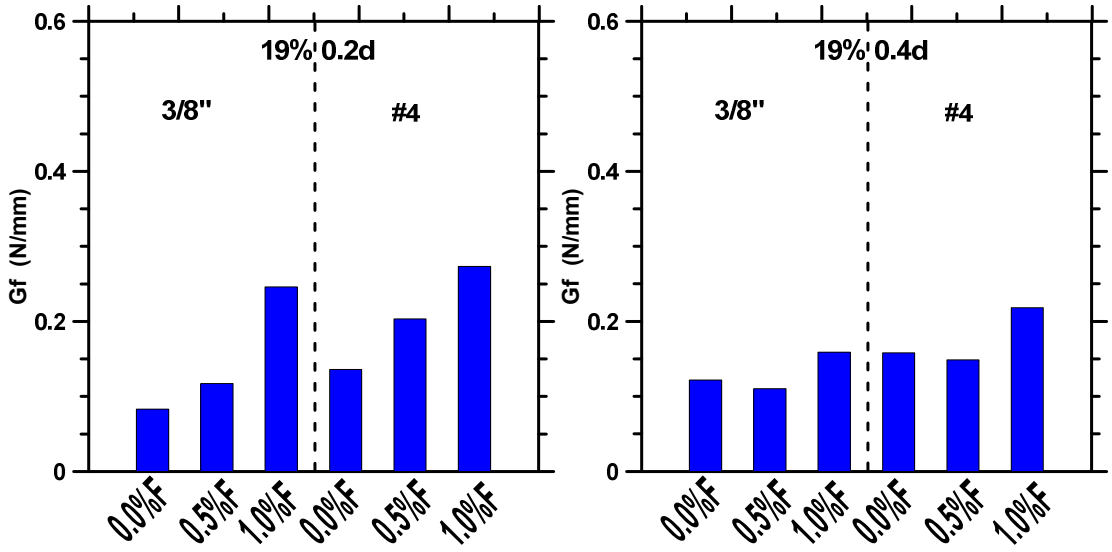

Figure 6-12: G_f at 19% porosity with a notch depth of (a) 0.2d and (b) 0.4d

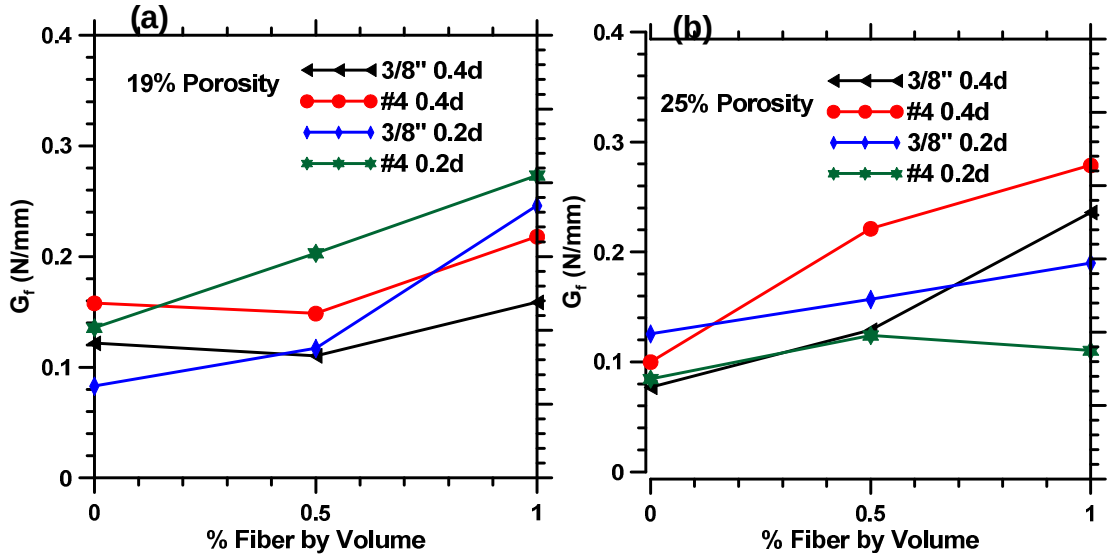

Figure 6-13: G_f vs. % fiber volume for (a) 19% porosity and (b) 25%

6.6 Summary

The fracture energy release rate and the toughness indices were calculated for the twelve different mix designs of pervious concrete. It was found that fracture energy release rate was highly dependent on porosity and fiber content but had little to no influence on pore size. The toughness indices which are representative of the residual strengths were determined for the pervious concrete specimens. It was found that these values were also highly dependent on porosity and fiber content.

7 CHAPTER 7: CONCLUSION

7.1 General

This chapter provides comprehensive conclusions based on the research carried out to investigate the influence of fibers and pore structure features on the mechanical and fracture properties of pervious concrete. Based on the research, several recommendations for further studies are also provided.

7.2 Permeability of Pervious Concretes and Human Teeth

This chapter has focused on studying the relationship between permeability and tortuosity as it pertains to porosity and pore size of pervious concrete. Various ideal geometric shapes were also constructed that had varying pore sizes and porosities. The pervious concretes also had differing pore sizes and porosities. The permeabilities were determined using three different methods; Stokes solver, Lattice Boltzmann method and the Katz-Thompson equation. These values were then compared to the tortuosity values determined using a Matlab code that uses a pore connectivity algorithm. The tortuosity was also determined from the inverse of the conductivity determined from a numerical analysis that was necessary for using the Katz-Thompson equation. These tortuosity values were then compared to the permeabilities. The pervious concretes and ideal geometric shapes showed consistent similarities between the tortuosities and the permeabilities.

Reconstruction of human teeth from actual SEM images of dentin and enamel were created and the permeabilities were determined using the Stokes solver and Lattice

Boltzmann method. These values were found to be consistent with empirical values found in literature.

7.3 Fracture Toughness

This topic has provided a fundamental understanding of the influence of the pore structure features and fibers on the fracture response of pervious concrete notched beams under three-point loading. The results from this study are expected to facilitate the material design of pervious concretes for adequate fracture resistance. Fibers generally were not found to influence the compressive strength to any significant degree, as is expected for conventional concretes also. Among the pore structure features, porosity exerted the maximum influence on compressive strength. For the pervious concretes evaluated in this study, it was found that the fracture toughness (K_{IC}) was primarily dependent on the porosity, even though K_{IC} was found to increase with increase in fiber volume fraction. For a given porosity, an increase in the pore size resulted in a reduction in the K_{IC} values. It was shown that, though the fibers are more effective at higher porosities, the overall benefits of having a lower porosity far outweigh this effect when K_{IC} values are considered. The critical crack length increased with increase in fiber volume irrespective of porosity and pore sizes.

The residual flexural capacity of the pervious concrete specimens were found to be invariant with porosity at a given fiber volume fraction. The contribution of fibers towards improving the residual flexural capacity was higher at a higher porosity (provided the pore size remained the same). In this case, there are more number of pores,

thereby reducing the mean free spacing between the pores. This increased the possibility that the pores are bridged by the fibers, resulting in the observed effect. The increased influence of fibers at higher porosity was also observed in the stress-crack extension relationship and in the R-curves.

A statistical model was used to express K_{IC} as a function of the pore structure features and fiber volume. The terms in the model were grouped and the model transformed to reduce the effects of multicollinearity. A stochastic simulation for sensitivity revealed that K_{IC} was mostly dependent on ϕ/τ. Since the tortuosity decreases with increasing porosity, the sensitivity of this term was amplified.

7.4 Fracture Energy

The fracture energy release rate and the toughness indices were calculated for the twelve different mix designs of pervious concrete. It was found that fracture energy release rate was highly dependent on porosity and fiber content but had little to no influence on pore size. The toughness indices which are representative of the residual strengths were determined for the pervious concrete specimens. It was found that these values were also highly dependent on porosity and fiber content.

7.5 Recommendations for Future Research

Future research involving different volume fractions of fibers, different porosities, and different aggregate sizes using the same test methods and analysis as described in this thesis is recommended. A more sophisticated model that relates the pore structure

features to the mechanical and fracture behavior of pervious concretes could be created. In this study only polypropylene fibers were used so using different materials such as steel and fiberglass would be good choices to study for further analysis.

LIST OF REFERENCES

Agar-Ozbek, A. S., Weerheijm, J., Schlangen, E., & van Breugel, K. (2013). Investigating porous concrete with improved strength: Testing at different scales. *Construction and Building Materials*, *41*, 480–490.

Amparano, F. E., Xi, Y., & Roh, Y.-S. (2000). Experimental study on the effect of aggregate content on fracture behavior of concrete. *Engineering Fracture Mechanics*, *67*(1), 65–84.

Armatas, G. S., Salmas, C. E., Louloudi, M., Androutsopoulos, G. P., & Pomonis, P. J. (2003). Relationships among Pore Size, Connectivity, Dimensionality of Capillary Condensation, and Pore Structure Tortuosity of Functionalized Mesoporous Silica. *Langmuir*, *19*(8), 3128–3136. doi:10.1021/la020261h

ASTM C 1018-97. (1997). Standard Test Method for Flexural Toughness and Firs-Crack Strength of Fiber-Reinforced Concrete (Using Beam With Third-Point Loading).

ASTM C1688/C1688M-13. (2009). Standard Test Method for Density and Void Content of Freshly Mixed Pervious Concrete.

Balendran, R. V., Zhou, F. P., Nadeem, A., & Leung, A. Y. T. (2002). Influence of steel fibres on strength and ductility of normal and lightweight high strength concrete. *Building and Environment*, *37*(12), 1361–1367.

Bazant, Z. P. (2002). Concrete fracture models: testing and practice. *Engineering fracture mechanics*, *69*(2), 165–205.

Bentz, D. P. (2008). Virtual pervious concrete: Microstructure, percolation, and permeability. *ACI Materials Journal*, *105*(3), 297.

Bentz, D. P., & Martys, N. S. (1994). Hydraulic radius and transport in reconstructed model three-dimensional porous media. *Transport in porous media*, *17*(3), 221–238.

Bentz, D. P., & Martys, N. S. (2007a). A Stokes Permeability Solver for Three-Dimensional Porous Media. National Institute of Standards and Technology.

Bentz, D. P., & Martys, N. S. (2007b, April). A Stokes Permeability Solber for Three-Dimensional Porous Media. NISTIR 7416 U.S. Deparment of Justice.

Berryman, J. G., & Blair, S. C. (1986). Use of digital image analysis to estimate fluid permeab ility of porous materials: Applicatio of two-point correlation functions. *Journal of Applied Physics*, 1930–1938.

Bieniek, A., & Moga, A. (2000). An efficient watershed algorithm based on connected components. *Pattern Recognition*, *33*(6), 907–916.

Bragov, A. M., Petrov, Y. V., Karihaloo, B. L., Konstantinov, A. Y., Lamzin, D. A., Lomunov, A. K., & Smirnov, I. V. (2013). Dynamic strengths and toughness of an ultra high performance fibre reinforced concrete. *Engineering Fracture Mechanics*. Retrieved from http://www.sciencedirect.com/science/article/pii/S0013794413000672

Chen, S., & Doolen, G. D. (1998). Lattice Boltzmann Method For Fluid Flows. *Annu. Rev. Fluid Mech.*, 329–363.

Coster, M., & Chermant, J.-L. (2001). Image analysis and mathematical morphology for civil engineering materials. *Cement & Concrete Composites*.

Deng, Z. (2005). The fracture and fatigue performance in flexure of carbon fiber reinforced concrete. *Cement & Concrete Composites*, 131–140.

Deo, Okar. (2010). *Influence of material structure on the structural and environmental properties of pervious concretes* (Dissertation). Clarkson University.

Deo, Omkar, & Neithalath, N. (2010). Compressive behavior of pervious concretes and a quantification of the influence of random pore structure features. *Materials Science and Engineering: A*, *528*(1), 402–412.

Deo, Omkar, & Neithalath, N. (2011). Compressive response of pervious concretes proportioned for desired porosities. *Construction and Building Materials*, *25*(11), 4181–4189.

Eissa, A.-B., & Batson, G. (1996). Model for predicting the fracture process zone and< i> R</i>-curve for high strength FRC. *Cement and Concrete Composites*, *18*(2), 125–133.

El-Dieb, A. S., & Hooton, R. D. (1994). Evaluation of the Katz-Thompson model for estimating the water permeability of cement-based materials from mercury intrusion porosimetry data. *Cement and concrete research*, *24*(3), 443–455.

Elices, M., & Rocco, C. G. (2008). Effect of aggregate size on the fracture and mechanical properties of a simple concrete. *Engineering fracture mechanics*, *75*(13), 3839–3851.

Epstein, N. (1989a). On toruosity and the tortuosity factor in flow and diffusion through porous media. *Chemical Engineering Science*.

Epstein, N. (1989b). On tortuosity and the tortuosity factor in flow and diffusion through porous media. *Chemical engineering science*, *44*(3), 777–779.

Garboczi, E. J., Bentz, D. P., & Martys, N. S. (1999). 1. Digital Images and Computer Modeling. *Experimental methods in the physical sciences*, *35*, 1–41.

Gokhale, A. M., Tewari, A., & Garmestani, H. (2005). Constraints on microstructural two-point correlation functions. *Scripta materialia*, *53*(8), 989–993.

Gopalaratnam, V. S., Shah, S. P., Batson, G. B., Criswell, M. E., Ramakrishnan, V., & Wecharatana, M. (1991). Fracture toughness of fiber reinforced concrete. *ACI Materials Journal*, *88*(4), 339–353.

Haselbach, L. M., Valavala, S., & Montes, F. (2006). Permeability predictions for sand-clogged Portland cement pervious concrete pavement systems. *Journal of environmental management*, *81*(1), 42–49.

He, X., & Luo, L. S. (1997). Theory of the lattice Boltzmann method: From the Boltzmann equation to the lattice Boltzmann equation. *Physical Review E*, *56*(6), 6811.

Hillerborg, A., Modeer, M., & Petersson, P.-E. (1976). Analysis of crack formation and crack growth in concrete by means of fracture mechanics and finite elements. *Cement and concrete research*, *6*(6), 773–781.

Hosmer Jr, D. W., Lemeshow, S., & May, S. (2011). *Applied survival analysis: regression modeling of time to event data* (Vol. 618). Wiley-Interscience. Retrieved from http://books.google.com/books?hl=en&lr=&id=IvvOopIqzWsC&oi=fnd&pg=PT9&dq=applied+survival+analysis&ots=ZtdYxaYXgm&sig=tiD2SF2q1_dT8ndSpZqF3iopVfI

HU, J. (2004). *Porosity of Concrete Morphological Study of Model Concrete*. Wuhan University of Technology, geboren te Danjiangkou, Hubei Province, P.R. China.

Huang, B., Wu, H., Shu, X., & Burdette, E. G. (2010). Laboratory evaluation of permeability and strength of polymer-modified pervious concrete. *Construction and Building Materials*, *24*(5), 818–823.

Jansen, D. C., Weiss, W. J., & Schleuchardt, S. H. (2000). Modified testing procedure for the two parameter fracture model for concrete. In *The Proceedings of the 14th Engineering Mechanics Conference (EM2000): Austin, TX*. Retrieved from http://digitalcommons.calpoly.edu/cgi/viewcontent.cgi?article=1125&context=cenv_fac

Jenq, Y. S., & Shah, S. P. (1985). A fracture toughness criterion for concrete. *Engineering Fracture Mechanics*, *21*(5), 1055–1069.

Jenq, Y., & Shah, S. P. (1985). Two parameter fracture model for concrete. *Journal of Engineering Mechanics*, *111*(10), 1227–1241.

Kevern, J. T., Schaefer, V. R., Wang, K., & Suleiman, M. T. (2008). Pervious concrete mixture proportions for improved freeze-thaw durability. *Journal of ASTM International*, *5*(2), 12.

Koleva, D. A., de Wit, J. H. W., van Breugel, K., Veleva, L. P., van Westing, E., Copuroglu, O., & Fraaij, A. L. A. (2008). Correlation of microstructure, electrical properties and electrochemical phenomena in reinforced mortar. Breakdown to multi-phase interface structures. Part II: Pore network, electrical properties and electrochemical response. *Materials characterization*, *59*(6), 801–815.

Kosuge, S. (2008). Model Boltzmann equation for gas mixtures: Construction and numerical comparison. *European Journal of Mechanics B/Fluids*, 170–184.

Kruskal, W. H. (1957). Historical notes on the Wilcoxon unpaired two-sample test. *Journal of the American Statistical Association*, *52*(279), 356–360.

Kumar, T. K. (1987). Multicollinearity in regression analysis. *The Review of Economics and Statistics*, *57*(3), 365–66.

Kutay, M. E. (2005). *Modeling Moisture Transport in Asphault Pavements*. University of Maryland.

Latour, L. L., Kleinberg, R. L., Mitra, P. P., & Sotak, C. H. (1995). Pore-Size Distributions and Tortuosity Heterogeneous Porous Media. *Journal Magnetic Resonance*, 83–91.

Liddel, C. M., Summers, C. J., & Gokhale, A. M. (2003). Stereological estimation of the morphology distribution of ZnS clusters for photonic crystal applications. *Materials Characterization*, *50*, 69–70.

Lin, Z., & Li, V. C. (1997). Crack bridging in fiber reinforced cementitious composites with slip-hardening interfaces. *Journal of the Mechanics and Physics of Solids*, *45*(5), 763–787.

Liu, D.-M. (1997). Influence of porosity and pore size on the compressive strength of porous hydroxyapatite ceramic. *Ceramics International*, *23*(2), 135–139.

Llorca, J., & Elices, M. (1990). Fracture resistance of fiber-reinforced ceramic matrix composites. *Acta metallurgica et materialia*, *38*(12), 2485–2492.

Mangan, A. P., & Whitaker, R. T. (1999). Partitioning 3D surface meshes using watershed segmentation. *Visualization and Computer Graphics, IEEE Transactions on*, *5*(4), 308–321.

Manning, D. G., & Hope, B. B. (1971). The effect of porosity on the compressive strength and elastic modulus of polymer impregnated concrete. *Cement and Concrete Research*, *1*(6), 631–644.

Marolf, A., Neithalath, N., Sell, E., Wegner, K., Weiss, J., & Olek, J. (2004). Influence of aggregate size and gradation on acoustic absorption of Enhanced Porosity Concrete. *ACI Materials Journal*, *101*(1), 82–91.

McKnight, P. E., & Najab, J. (2010). Mann-Whitney U Test. *Corsini Encyclopedia of Psychology*. Retrieved from http://onlinelibrary.wiley.com/doi/10.1002/9780470479216.corpsy0524/full

Michielsen, K., & De Raedt, H. (2000). Morphological image analysis. *Computer Physics Communications*, 94–103.

Mobasher, B., & Peled, M. (2004). Use of R-Curves for Characterization of Toughening in Fiber Reinforced Concrete. Presented at the , International Conference on Fracture Mechanics of Concrete and Concrete Structures(FraMCoS-V), Vail, Colorado.

Mouret, M., Ringot, E., & Bascoul, A. (2001). Image analysis: a tool for the characterisation of hydration of cement in concrete-metrological aspects of magnification on measurement. *Cement and Concrete Composites*, *23*(2-3), 201–206.

Neithalath, N., Bentz, D. P., & Sumanasooriya, M. S. (2010). Predicting the Permeability of Pervious Concrete: Advances in characterization of pore structure and transport properties. *Concrete International*, 35–40.

Neithalath, N., Marolf, A., Weiss, J., & Olek, J. (2005). Modeling the influence of pore structure on the acoustic absorption of enhanced porosity concrete. *Journal of Advanced Concrete Technology*, *3*(1), 29–40.

Neithalath, N., Sumanasooriya, M. S., & Deo, O. (2010). Characterizing pore volume, sizes, and connectivity in pervious concretes for permeability prediction. *Materials characterization*, *61*(8), 802–813.

Neithalath, N., Weiss, J., & Olek, J. (2006). Characterizing enhanced porosity concrete using electrical impedance to predict acoustic and hydraulic performance. *Cement and Concrete Research*, *36*(11), 2074–2085.

Olejniczak, A. J., Smith, T. M., Feeney, R. N., Macchiarelli, R., Mazurier, A., Bondioli, L., … Garcia-Tabernero, A. (2008). Dental tissue proportions and enamel thickness in Neandertal and modern human molars. *Journal of human evolution*, *55*(1), 12–23.

Olek, J., Weiss, W. J., Neithalath, N., Marolf, A., Sell, E., & Thornton, W. D. (2003). *development of quiet and durable porous Portland cement concrete paving materials* (pp. 1–179). Retrieved from http://trid.trb.org/view.aspx?id=698009

Poole, D. F. G., Newman, H. N., & Dibdin, G. H. (1981). Structure and porosity of human cervical enamel studied by polarizing microscopy and transmission electron microscopy. *Archives of oral biology*, *26*(12), 977–982.

Reis, J. M. L. (2006). Fracture and flexural characterization of natural fiber-reinforced polymer concrete. *Construction and Building Materials*, *20*(9), 673–678.

Report on Pervious Concrete (ACI 522R – 10). (2010). In *2.ACI Committee 522, ACI 522R – 10* (p. 42). Presented at the American Cocrete Institute.

ROY, D. M., & GOUDA, G. R. (1973). Porosity-Strength Relation in Cementitious Materials with Very High Strengths. *Journal of the American Ceramic Society*, *56*(10), 549–550.

Saleh, A. L. (1997). *Crack Growth in Concrete Using Boundary Elements* (Vol. 30). Computational Mechanics Publications.

Sanford, R. J. (2003). *Principles of Fracture Mechanics*. Prentice Hall.

Shah, S. P., Swartz, S. E., & Ouyang, C. (1995). *Fracture Mechanics of Concrete: Applications of Fracture Mechanics To Concrete, Rock, and Other Quasi-Brittle Materials*. John Wiley & Sons, Inc.

Soroushian, P., & Elzafraney, M. (2005). Morphological operations, planar mathematical formulations, and stereological interpretations for automated image analysis of concrete microstructure. *Cement and Concrete Composites*, *27*, 823–833.

Stjernberg, K. G. (1969). Determination of Volume Distribution Function by Lineal Analysis. *Metallography*, *2*, 161–170.

Sumanasooriya, M., Bentz, D. P., & Neithalath, N. (2010). Planar Image-Based Reconstruction of Pervious Concrete Pore Structure and Permeability Prediction. *ACI Materials Journal*, 1–9.

Sumanasooriya, M., & Neithalath, N. (2009). Stereology-and Morphology-Based Pore Structure Descriptors of Enhanced Porosity (Pervious) Concrete. *ACI Materials Journal*, *September-October*, 429–438.

Sumanasooriya, M. S, & Neithalath, N. (2011). Pore structure features of pervious concretes proportioned for desired porosities and their performance prediction. *Cement and Concrete Composites*, 778–787.

Sumanasooriya, Milani S., Deo, O., & Neithalath, N. (2009). Computational prediction of elastic properties of enhanced porosity concretes using 3D reconstructed images (pp. 275–289). Presented at the Proceedings of 9th Brittle Matrix Composites, Warsaw, Poland.

Sumanasooriya, Milani S., Deo, O., & Neithalath, N. (2012). Particle Packing-Based Material Design Methodology For Pervious Concretes. *ACI Materials Journal*, *109*(2), 205–214.

Tennis, P. D., Leming, M. L., & Akers, D. J. (2004). *Pervious concrete pavements*. Portland Cement Association Skokie, IL. Retrieved from http://myscmap.sc.gov/marine/NERR/pdf/PerviousConcrete_pavements.pdf

Tjiptobroto, P., & Hansen, W. (1993). Tensile strain hardening and multiple cracking in high-performance cement-based composites containing discontinuous fibers. *ACI Materials Journal*, *90*(1). Retrieved from http://www.concrete.org/PUBS/JOURNALS/OLJDetails.asp?Home=MJ&ID=4031

Torquato, S. (2001). *Random heterogeneous materials: microstructure and macroscopic properties* (Vol. 16). Springer. Retrieved from http://books.google.com/books?hl=en&lr=&id=PhG_X4-8DPAC&oi=fnd&pg=PA1&dq=Random+Heterogeneous+Materials+%E2%80%

93+Microstructure+and+Macroscopic+Properties&ots=SY79uYe2nP&sig=Unf7-rB3HPM-K8VtUM9Gn5bkqUQ

Tumidajski, P. J., & Lin, B. (1998). On the validity of the Katz-Thompson equation for permeabilities in concrete. *Cement and concrete research*, *28*(5), 643–647.

Usami, S., Kimoto, H., Takahashi, I., & Shida, S. (1986). Strength of ceramic materials containing small flaws. *Engineering fracture mechanics*, *23*(4), 745–761.

Vennat, E., Aubry, D., & Degrange, M. (2010). Collagen fiber network infiltration: permeability and capillary infiltration. *Transport in porous media*, *84*(3), 717–733.

Vervoort, R. W., & Cattle, S. R. (2003). Linking hydraulic conductivity and tortuosity parameters to pore space geometry and pore-size distribution. *Journal of Hydrology*, *272*(1-4), 36–49.

Wittmann, F. H. (2002). Crack formation and fracture energy of normal and high strength concrete. *Sadhana*, *27*(4), 413–423.

Yang, J., & Jiang, G. (2003). Experimental study on properties of pervious concrete pavement materials. *Cement and Concrete Research*, *33*(3), 381–386.

Ye, G., Hu, J., Van Breugel, K., & Stroeven, P. (2002). Characterization of the development of microstructure and porosity of cement-based materials by numerical simulation and ESEM image analysis. *Materials and Structures*, *35*(10), 603–613.

Zhang, Z., & Ansari, F. (2006). Fracture mechanics of air-entrained concrete subjected to compression. *Engineering fracture mechanics*, *73*(13), 1913–1924.

Zhou, J. G. (2010). Rectangular lattice Boltzmann method. *Physical Review E*, *81*(2). doi:10.1103/PhysRevE.81.026705